J. Fluid Mech. (2019), *vol.* 874, *pp.* 38–75. © Cambridge University Press 2019
doi:10.1017/jfm.2019.434

Topology-based characterization of compressibility effects in mixing layers

S. Arun[1], A. Sameen[1,†], B. Srinivasan[2] and S. S. Girimaji[3]

[1]Department of Aerospace Engineering, Indian Institute of Technology Madras, Chennai, 600036, India

[2]Department of Mechanical Engineering, Indian Institute of Technology Madras, Chennai, 600036, India

[3]Department of Ocean Engineering, Texas A&M University, College Station, TX 77843, USA

(Received 4 December 2018; revised 23 May 2019; accepted 23 May 2019;
first published online 3 July 2019)

Direct numerical simulations of high-speed mixing layers are used to characterize the effects of compressibility on the basis of local streamline topology and vortical structure. Temporal simulations of the mixing layers are performed using a finite volume gas-kinetic scheme for convective Mach numbers ranging from $M_c = 0.2$ to $M_c = 1.2$. The focus of the study is on the transient development and the main objectives are to (i) investigate and characterize the turbulence suppression mechanism conditioned upon local streamline topology; and (ii) examine changes in the vortex vector field – distribution, magnitude and orientation – as a function of Mach number. We first reaffirm that kinetic energy suppression with increasing Mach number is due to a decrease in pressure–strain redistribution. Then, we examine the suppression mechanism conditioned upon topology and vortex structure. Conditional statistics indicate that (i) at a given Mach number, shear-dominated topologies generally exhibit more effective pressure–strain redistribution than vortical topologies; and (ii) for a given topology, the level of pressure–strain correlation mostly decreases with increasing Mach number. At each topology, with increasing Mach number, there is a corresponding decrease in turbulent shear stress and production leading to reduced kinetic energy. Further, as M_c increases, the proportion of vortex-dominated regions in the flow increases, leading to further reduction in the turbulent kinetic energy of the flow. Then, the orientation of vortical structures and direction of fluid rotation are examined using the vortex vector approach of Tian *et al.* (*J. Fluid Mech.*, vol. 849, 2018, pp. 312–339). At higher M_c, the vortex vectors tend to be more aligned in the streamwise direction in contrast to low M_c wherein larger angles with streamwise direction are preferred. The connection between vortex orientation and kinetic energy production is also investigated. The findings lead to improved insight into turbulence suppression dynamics in high Mach number turbulent flows.

Key words: compressible turbulence, shear layer turbulence

1. Introduction

Free shear layer flows and associated turbulence have been extensively studied using analytical, experimental and numerical techniques for several decades. The planar

† Email address for correspondence: sameen@ae.iitm.ac.in

mixing layer is the simplest of them with a modal instability, devoid of the complexities of most other shear flows. As Mach number of the flow increases, compressibility effects become significant and begin to influence the flow dynamics. These effects in a mixing layer are quantified by the convective Mach number, $M_c = (U_1 - U_2)/(c_1 + c_2)$, where U_1, U_2 are free-stream velocities and c_1, c_2 are sonic speeds in either stream. The most notable effect of compressibility on mixing layers is the suppression of turbulence and the consequent reduction of spreading rate. The physical mechanism of turbulence suppression due to compressibility has been examined in previous works. It has also been noted that the turbulent flow structure is modified due to compressibility (Normand & Lesieur 1992). The goal of the present study is to enhance the understanding of compressibility effects by characterizing the suppression mechanism in terms of local streamline topology and vortex structure.

The reduced turbulence levels and mixing-layer spread rate at high M_c are attributed to the suppression of pressure–strain redistribution by Pantano & Sarkar (2002). As Mach number increases, the free-stream pressure itself decreases, leading to reduced levels of pressure fluctuations and a proportional reduction in pressure–strain correlation. Recent attempts to explain the reduction of growth rate by compressibility include a detailed analysis of vorticity and its generation near the turbulent/non-turbulent interface and the entrainment process. Jahanbakhshi & Madnia (2016) show that the curvature of the turbulent/non-turbulent interface in mixing layers is significantly altered by compressibility, thereby leading to a reduction in entrained mass flux. Karimi & Girimaji (2016) examine the stabilizing action of compressibility on Kelvin–Helmholtz instability and propose the existence of a dilatation interface layer (DIL) in which strong vorticity wind and unwind due to the action of pressure field. This reversal of vorticity in time reduces the growth of instability. Linear stability analysis by Sandham & Reynolds (1990) shows that it is not just the growth rate, but the most unstable mode itself is modified by compressibility. The most unstable mode changes to oblique modes for $M_c > 0.6$, leading to strongly three-dimensional structures at higher Mach numbers. Karimi & Girimaji (2017) also exhibit the effect of perturbation orientation on instability growth in compressible mixing layers. It is demonstrated that the degree of stabilization decreases with increasing obliqueness. Bertsch, Suman & Girimaji (2012) investigate the effects of flow-thermodynamic interactions in compressible homogeneous shear flows by examining the evolution of pressure fluctuations. The analysis suggests that in spatio-temporally developing flows, compressibility effects diminish with time (or distance). Thus, compressibility effects are most severe in the transient stages of flow evolution. In this paper, we address the effects of compressibility on the turbulence statistics and examine the role of pressure and inertia effects during the transient evolution of mixing layers.

In recent years, characterization of turbulence and turbulent mechanisms using local streamline topology has gained much popularity (Chong, Perry & Cantwell 1990). Soria *et al.* (1994) studied the local topology in incompressible mixing layers using this technique and identify flow features such as vortex sheets and vortex tubes. Compressibility effects on local flow topology were examined by Suman & Girimaji (2010) in decaying isotropic turbulence. Although the Mach number has little effect, the topology was found to be sensitive to local dilatation. Vaghefi & Madnia (2015) observe that the topology in the vicinity of a turbulent/non-turbulent interface is different from that in the turbulent core of a mixing layer and that vorticity is concentrated in specific topologies.

Vortical eddy structures play a key role in many turbulent flows, but a comprehensive examination of these structures is rendered difficult due to the lack of a formal

mathematical basis for identifying them. There have been attempts to define a vortex using both Eulerian and Lagrangian approaches (Epps 2017). Several vortex identification techniques using velocity gradient tensor have been proposed over the years, of which the Q-criterion by Hunt, Wray & Moin (1988) and the λ_2-criterion by Jeong & Hussain (1995) are widely used. Tian *et al.* (2018) propose a vector quantity to identify vortical structures in the flow field, which not only quantifies the local strength of rotation of a fluid element but also provides the direction of rotation. Vortex identification techniques help to elucidate the large-scale structures in the flow field. Compressibility effects on flow structures and their relation to turbulence statistics in compressible boundary layers are examined by Normand & Lesieur (1992), Wang & Lu (2012). The large-scale organization in mixing layers is influenced by the compressibility as observed by Sandham & Reynolds (1990) and Sandham & Reynolds (1991). At high M_c, the spanwise roller structures are mostly absent, and the vortical structures are elongated in the streamwise direction, which leads to different mixing characteristics. Jahanbakhshi, Vaghefi & Madnia (2015) find that the interaction of intense vorticity structures with the turbulent/non-turbulent interface is crucial to vorticity transport in compressible mixing layers. In direct numerical simulations (DNS) of spatially evolving mixing layers by Zhou, He & Shen (2012), it is observed that Λ-structures in the flow field evolve to hairpin vortices which eventually break down to slender vortices before the flow reaches a self-similar state. Pirozzoli *et al.* (2015) also observe that a spanwise coherence in flow structures makes way for skewed eddies in the flow which align in the flow direction. Reynolds stress and mean velocity profiles in these cases also evolve with time and are related to the evolution of large-scale structures. In compressible homogeneous shear flow, production and turbulent kinetic energy are predominant in strain-dominated topologies, as shown by Ma & Xiao (2016) using conditional statistics of DNS data. While the changes in flow structures due to compressibility have been studied to a reasonable extent, the relation between vortex-structure modification and changes in flow mechanisms is yet to be clearly established.

The objective of this work is to develop further insight into the turbulence suppression due to compressibility effects in high-speed mixing layers. Specifically, we seek to characterize the suppression mechanism conditioned on local streamline topology and vortical structure. To this end, we undertake the following tasks:

(i) Perform mixing-layer simulations over a range of Mach numbers that encompasses incompressible and compressible flow regimes.
(ii) Reaffirm the suppression of turbulence and mixing-layer spread rate with increasing Mach number.
(iii) Establish the changes, with increasing Mach number, in pressure–strain correlation, turbulence shear stress and kinetic energy production processes when conditioned upon local streamline topology.
(iv) Examine the changes in vortex structure with increasing Mach numbers. We quantify the change in topology by means of the vortex field structure.

Flow configuration and simulation parameters are summarized in § 2. The main results, including the evolution of turbulent quantities and topology effects, are discussed in § 3, followed by conclusions in § 4.

2. Numerical set-up

We perform simulations of temporally evolving mixing layers in a cuboid domain, shown in figure 1, with free-stream velocities in the $\pm x_1$ direction. The streamwise

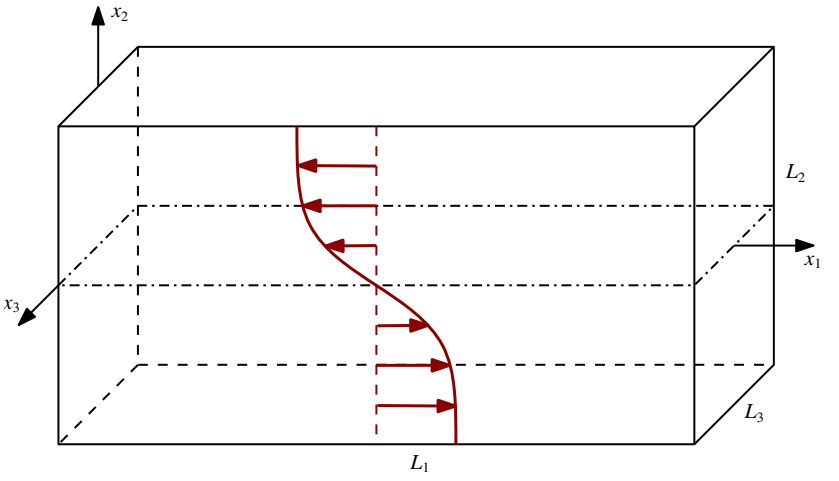

FIGURE 1. (Colour online) Schematic of the computational domain with mean velocity profile.

Case	M_c	L_1/δ_{θ_0}	L_2/δ_{θ_0}	L_3/δ_{θ_0}	Re_ω	Re_λ	M_t	l_1/L_1	l_η/Δ
M2	0.20	314.16	157.08	78.54	8495	126	0.098	0.029	0.415
M5	0.50	314.16	157.08	78.54	8273	108	0.208	0.034	0.418
M7	0.75	314.16	157.08	78.54	8160	107	0.302	0.032	0.441
M9	0.90	314.16	157.08	78.54	9544	104	0.362	0.073	0.442
M12	1.20	314.16	157.08	78.54	11 112	107	0.362	0.076	0.465

TABLE 1. Key non-dimensional parameters at the end of the simulations for different cases.

velocity is a function of the transverse location (x_2). The domain, of dimension $L_1 \times L_2 \times L_3$ (see table 1), is discretized uniformly into $512 \times 256 \times 128$ grid points with periodic boundary conditions in the streamwise (x_1) and spanwise (x_3) directions. In the transverse direction, stress-free boundary conditions are applied. A discussion on domain independence and grid convergence is given in § A.2.

Simulations are performed for five different values of convective Mach number, $M_c = (0.2,\ 0.5,\ 0.75,\ 0.9,\ 1.2)$. The lowest M_c case corresponds to a nearly incompressible case, while the two higher Mach number cases have significant compressibility effects involved. A key parameter used for initializing the flow field is the initial momentum thickness, δ_{θ_0}. The Reynolds number of the flow is defined based on free-stream velocity difference and momentum thickness ($Re = \rho_\infty \Delta U \delta_{\theta_0}/\mu$). For all cases considered here initial $Re = 160$. Many authors have used $Re \approx 200$ (Jahanbakhshi *et al.* 2015; Vaghefi & Madnia 2015) in their simulations, and the Reynolds number used in the present simulations is well documented (Pantano & Sarkar 2002; Foysi & Sarkar 2010; Hadjadj, Yee & Sjögreen 2012). Mean streamwise velocity has a hyperbolic tangent profile given by

$$\tilde{u}_1 = \frac{1}{2}\Delta U \tanh\left(\frac{-x_2}{2\delta_{\theta_0}}\right), \tag{2.1}$$

and the other two components are set to zero. Temperature follows the Crocco–Busemann relation (White 2006) for compressible shear layers,

$$\frac{\tilde{T}(x_2)}{T_\infty} = 1 + \frac{\gamma - 1}{2} M_c^2 \left[1 - \left(\frac{\tilde{u}_1(x_2)}{\Delta U} \right)^2 \right], \tag{2.2}$$

where $\tilde{u_1}$ and $\tilde{T}$ are Favre-averaged quantities defined in the next section. The pressure field is uniform, and the density field is obtained from the ideal gas equation of state. Three-dimensional perturbations are added to the mean velocity field to accelerate the transition to turbulence. Perturbations are generated using a digital filter method, which has been successfully employed in the computation of temporally evolving mixing layers by Vaghefi & Madnia (2015). By this method, three-dimensional perturbations are generated based on a prescribed length scale and Reynolds stress profile. A spatially correlated perturbation field, rather than white noise, is obtained by employing this technique. We used initial vorticity thickness ($\delta_{\omega_0} \approx 4\delta_{\theta_0}$) as length scale and Gaussian profiles for Reynolds stress components, with peak values of stress components from the nearly incompressible case of Pantano & Sarkar (2002). All simulations are initialized with the same perturbation velocity field to minimize differences due to initial condition effects on the transient evolution of the mixing layer. Therefore, any difference in the evolution of the mixing layer is the varying response of the system relaxing from these initial conditions and is due to compressibility, as M_c is the only parameter which varies across the different cases.

A finite volume gas-kinetic scheme which solves the Bhatnagar–Gross–Krook (BGK)-Boltzmann equation is used for computations (Xu, Mao & Tang 2005). The scheme employs a second-order approximation for the variation of particle velocity distribution function in space. For the simulation of turbulent flows, Kumar, Girimaji & Kerimo (2013) observed that macroscopic variable reconstruction using weighted essentially non-oscillatory (WENO) schemes enable the resolution of sharp discontinuities like shocklets without compromising on the accuracy in smooth flow regions. Following their work, a fifth-order WENO reconstruction is used to calculate cell interface quantities. To enable simulations for gases with $Pr \neq 1$, a Prandtl number correction, proposed by May, Srinivasan & Jameson (2007), is employed. Time step is determined according to the Courant–Friedrichs–Lewy (CFL) criterion using macroscopic flow variables. A brief discussion on the numerical scheme is given in § A.1.

3. Results

The turbulent statistics are discussed for different cases to understand how they vary with convective Mach number, which is a measure of compressibility. Following that, we analyse how these statistics are distributed across different topologies in the flow, in an attempt to explain how changes in topology with Mach number influence the turbulent statistics. A density weighted averaging in homogeneous x_1x_3 plane is used to obtain mean velocity and temperature. Mean density and pressure fields are obtained by Reynolds averaging. We use the conventional notations for Reynolds ($\overline{[.]}$) and Favre ($\tilde{[.]}$) averaged quantities and respective fluctuations ($[.]'$ and $[.]''$) from averages, as given in equation (3.1).

$$\rho = \bar{\rho} + \rho', \quad p = \bar{p} + p', \tag{3.1a,b}$$

$$\tilde{u} = \overline{\rho u}/\bar{\rho}, \quad u = \tilde{u} + u'', \tag{3.1c,d}$$

$$\tilde{T} = \overline{\rho T}/\bar{\rho}, \quad T = \tilde{T} + T'', \tag{3.1e,f}$$

3.1. *Validation*

Our computational results are validated by comparing the temporal evolution of the mixing-layer width with existing experimental and numerical data. Suppression of mixing-layer growth rate by compressibility is a well-known phenomenon, and a vast majority of the literature on compressible mixing layers focuses on this aspect. We use momentum thickness (δ_θ), an integral quantity, to quantify the extent of the shear layer. Evolution of momentum thickness, normalized by its initial value (δ_{θ_0}), with time ($\tau = \Delta U t/\delta_{\theta_0}$) is shown in figure 2(*a*) for different M_c. After an initial transient period, the mixing layer has a self-similar evolution characterized by a linear growth of momentum thickness. The linear growth rates, which reduce with Mach number, are shown in figure 2(*b*). Self-similar growth rate, $\dot{\delta}$, normalized by the incompressible growth rate ($\dot{\delta}_{inc}$) is plotted along the vertical axis against convective Mach number on the horizontal axis. Growth rate at the lowest M_c is chosen as the incompressible growth rate and is estimated to be $\dot{\delta}_{inc} = 0.0167$, which is in good agreement with the accepted value of $\dot{\delta}_{inc} = 0.0160$ (Pantano & Sarkar 2002). The self-similar growth rates for different M_c are compared with the empirical models of Birch & Eggers (1972), Slessor, Zhuang & Dimotakis (2000) and Barone, Oberkampf & Blottner (2006) in figure 2(*b*). Growth rates from several numerical simulations are also compared in the same figure, and they show a scattered behaviour, which is attributed to differences in initial conditions and the reference value chosen as the incompressible growth rate. As further validation of our results, we show the evolution of anisotropy tensor for different M_c in figure 3. The anisotropy tensor (b_{ij}) is defined as

$$b_{ij} = \frac{\bar{R}_{ij} - \frac{2}{3}\bar{K}\delta_{ij}}{2\bar{K}}, \tag{3.2}$$

where $\bar{R}_{ij}$ and $\bar{K}$ are respectively Reynolds stress and turbulent kinetic energy integrated across the mixing layer. The evolution of anisotropy tensor (b_{11}, b_{22}, b_{12}) at $M_c = 0.20$, 0.75 and 1.20 from our computations are compared against the results of Pantano & Sarkar (2002). However, their computations are for different Mach numbers, and our results are compared against the evolution of anisotropy for $M_c = 0.3$, 0.7 and 1.1 from Pantano & Sarkar (2002). The mean velocity gradient is negative according to equation (2.1), which implies that the Reynolds shear stress R_{12}, and hence b_{12}, is positive in our simulations. Anisotropy peaks during the initial period before it settles down to a lower value, which increases marginally with M_c. While the late time anisotropy levels from our computations match well with those in the literature, there is a difference in the peak values. This can be attributed to the differences in setting up the initial perturbation field. The peak value of u''_{1rms}/u''_{2rms} for M02 is 1.24, which is in agreement with previous numerical experiments (Gatski & Bonnet 2013).

It is important that the small scales are resolved in turbulent flow computations. If the smallest length scale in the flow, which is the Kolmogorov length scale, is of the same order as the grid size then the scales are sufficiently resolved. The Kolmogorov scale (l_η) is a function of turbulent energy dissipation and kinematic viscosity and takes the smallest value where dissipation is maximum, which is at the centreline of the mixing layer. In table 1, we report the Reynolds number based on vorticity thickness (Re_ω; $\delta_\omega = \Delta U/(\mathrm{d}\tilde{u}_1/\mathrm{d}x_2)_{max}$), Taylor microscale Reynolds number ($Re_\lambda = 2K\sqrt{5/3\nu\epsilon}$), turbulent Mach number ($M_t = \sqrt{2\bar{\rho}K/\gamma\bar{p}}$) and Kolmogorov length scale (l_η/δ) at the end of the simulation for each case. The grid size (Δ), shown to be

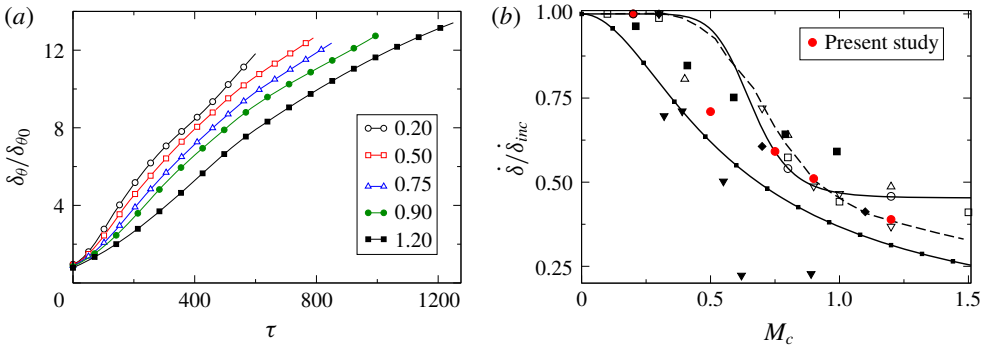

FIGURE 2. (Colour online) (*a*) Evolution of momentum thickness for various M_c. (*b*) Comparison of linear growth rates at different Mach numbers with different numerical databases and empirical models. ▼, Papamoschou & Roshko (1988); ■, Freund, Lele & Moin (2000); ◆, Pantano & Sarkar (2002); △, Fu & Li (2006); ▽, Foysi & Sarkar (2010); □, Hadjadj *et al.* (2012); ○, Vaghefi *et al.* (2013); (- - -), Birch & Eggers (1972); (—▪—), Slessor *et al.* (2000); (——), Barone *et al.* (2006).

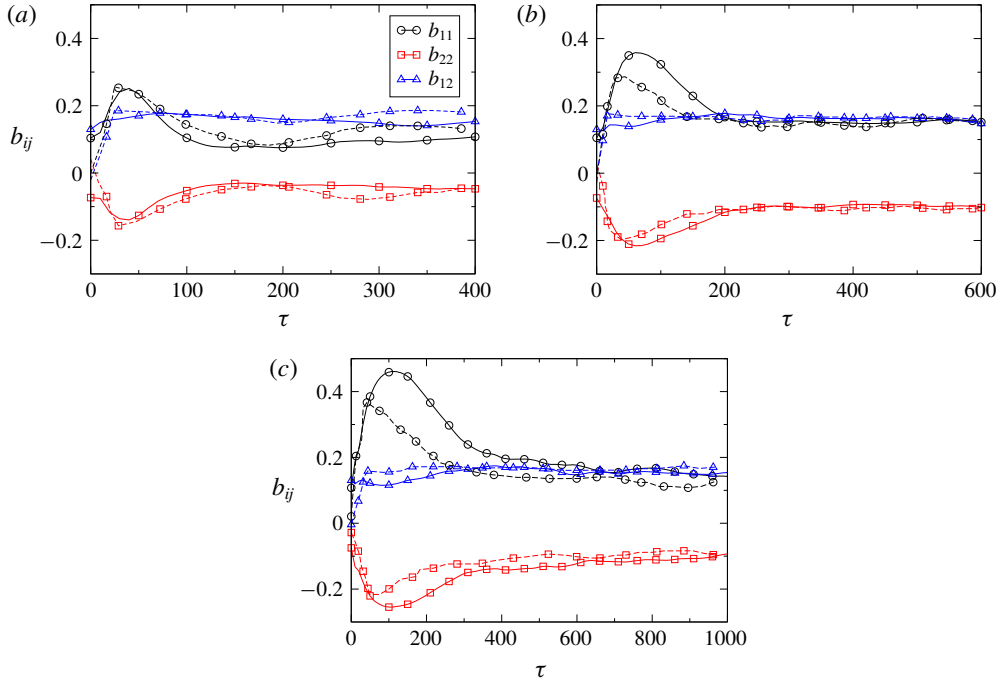

FIGURE 3. (Colour online) Evolution of anisotropy tensor for (*a*) $M_c = 0.20$, (*b*) $M_c = 0.75$ and (*c*) $M_c = 1.20$. Dashed lines in (*a–c*) correspond to anisotropy levels at $M_c = 0.3, 0.7$ 1.1 reported by Pantano & Sarkar (2002).

comparable with Kolmogorov scales, is small enough to resolve all the scales. We also compute the integral length scale (l_1), defined as

$$l_1 = \frac{1}{\overline{u_1''^2}} \int_0^{L_1/2} \overline{u_1''(\boldsymbol{x}) u_1''(\boldsymbol{x} + \delta\hat{e}_1)}\, \mathrm{d}\delta, \tag{3.3}$$

where the separation (δ) is along the streamwise direction ($\hat{e}_1$). At the end of the simulation, it is observed that the large scales, quantified by l_1, are very small compared to domain length, thereby ensuring that the computations are not contaminated by domain size. A comparison of M_t at the centreline, a measure of compressibility, for the different cases shows that compressibility effects are negligible for the two low M_c cases. Turbulent Mach number increases with M_c, but the increase is not proportional to that in the convective Mach number.

3.2. *Evolution of turbulent statistics*

In the present study, we focus on the initial evolution of the mixing layers, during which the effects of compressibility, being significant, manifest in the slow growth of momentum thickness. Our objective is to investigate how compressibility changes different turbulent statistics during this initial period. The statistics reported in this work correspond to time, $\tau < 400$. Turbulent statistics in mixing layers are a function of the transverse direction, x_2, at any given instant of time. To enable comparison during transient evolution of the mixing layer, we use an averaged value for turbulent quantities defined as

$$F(t) = \frac{\int f(t, x_2)\,\mathrm{d}x_2}{\int \mathrm{d}x_2}, \tag{3.4}$$

where $f(t, x_2)$ is any turbulent statistic varying along the transverse direction and $F(t)$ is the corresponding averaged quantity. However, the definition does not hold any physical meaning if a quantity takes both positive and negative values across the shear layer and caution must be exercised while employing this method to various turbulent statistics. For example, the transport terms in the kinetic energy budget cannot be quantified using such an integrated value.

The Reynolds stress ($R_{ij} = \widetilde{u_i'' u_j''}$) transport equation for compressible turbulent flows is given by

$$\bar{\rho}\frac{DR_{ij}}{Dt} + \frac{\partial T_{ijk}}{\partial x_k} = \mathcal{P}_{ij} + \Pi_{ij} - \epsilon_{ij} + M_{ij}, \tag{3.5}$$

where

$$\mathcal{P}_{ij} = -\bar{\rho}\left[R_{ik}\frac{\partial \tilde{u}_j}{\partial x_k} + R_{jk}\frac{\partial \tilde{u}_i}{\partial x_k}\right], \tag{3.6a}$$

$$\Pi_{ij} = \overline{p'\left[\frac{\partial u_j''}{\partial x_i} + \frac{\partial u_i''}{\partial x_j}\right]}, \tag{3.6b}$$

$$\epsilon_{ij} = \overline{\sigma_{ik}'\frac{\partial u_j''}{\partial x_k}} + \overline{\sigma_{jk}'\frac{\partial u_i''}{\partial x_k}}, \tag{3.6c}$$

$$M_{ij} = \overline{\rho' u_i''}\left[\frac{\partial \bar{p}}{\partial x_j} - \frac{\partial \bar{\sigma}_{jk}}{\partial x_k}\right], + \overline{\rho' u_j''}\left[\frac{\partial \bar{p}}{\partial x_i} - \frac{\partial \bar{\sigma}_{ik}}{\partial x_k}\right], \tag{3.6d}$$

$$T_{ijk} = \overline{\rho u_i'' u_j'' u_k''} + \overline{p' u_j''}\delta_{ik} + \overline{p' u_i''}\delta_{jk} - \overline{\sigma_{ik}' u_j''} - \overline{\sigma_{jk}' u_i''}, \tag{3.6e}$$

are the production by mean flow gradient ($\mathcal{P}_{ij}$), pressure–strain correlation (Π_{ij}), viscous dissipation (ϵ_{ij}), fluctuating mass flux contribution ($\mathcal{M}_{ij}$) and transport (T_{ijk}).

The mean and fluctuating viscous stress tensors are respectively given by $\bar{\sigma}_{ij}$ and σ'_{ij}, of which the fluctuating part is from velocity fluctuations. Contributions due to viscosity fluctuations are negligible and hence discarded. A transport equation for turbulent kinetic energy is obtained from equation (3.5) by contracting the indices and is as follows,

$$\bar{\rho}\frac{DK}{Dt} + \frac{\partial T_k}{\partial x_k} = \mathcal{P} + \Pi - \epsilon + \mathcal{M}, \tag{3.7}$$

where $K = \frac{1}{2}\widetilde{u''_i u''_i}$ and the other terms $\mathcal{P}, \Pi, \epsilon, \mathcal{M}$ and T_k are similarly obtained from equations (3.6*a–e*), respectively.

$$\mathcal{P} = -\bar{\rho}R_{ik}\frac{\partial \tilde{u}_i}{\partial x_k}, \tag{3.8a}$$

$$\Pi = \overline{p'\frac{\partial u''_i}{\partial x_i}}, \tag{3.8b}$$

$$\epsilon = \overline{\sigma'_{ik}\frac{\partial u''_i}{\partial x_k}}, \tag{3.8c}$$

$$\mathcal{M} = \overline{\rho' u''_i}\left[\frac{\partial \bar{p}}{\partial x_i} - \frac{\partial \bar{\sigma}_{ik}}{\partial x_k}\right], \tag{3.8d}$$

$$T_k = \overline{\rho u''_i u''_i u''_k}/2 + \overline{p' u''_i}\delta_{ik} - \overline{\sigma'_{ik} u''_i}. \tag{3.8e}$$

In a temporal mixing layer, the mean velocity has only one non-zero component and all mean statistics vary only in the transverse direction. The various correlations described above in their general form reduce accordingly and are discussed in detail below.

Figures 4–6 show the evolution of turbulent kinetic energy, turbulent stress components and their budgets for cases M2, M7 and M12. Reynolds stress components and turbulent kinetic energy are normalized by ΔU^2 and budget quantities by $\Delta U^3/\delta_\theta(t)$. Only the dominant source (positive) and sink (negative) terms in the respective budget equations are shown in the plots. Evolution of averaged turbulent kinetic energy across the shear layer, for different M_c, is given in figure 4(*a*). Along the horizontal axis is non-dimensional time (τ) and along the vertical axis is averaged turbulent kinetic energy. For all cases, turbulent energy increases with time, but at slower rates for higher Mach numbers. This means that the turbulent fluctuations are suppressed by compressibility and this is in agreement with our knowledge of compressible mixing layers. The reason for the suppression can be understood by comparing the budgets of turbulent kinetic energy. The major contributions to the kinetic energy budget are from the production ($\mathcal{P}$), dissipation (ϵ) and transport of turbulent fluctuations (T_k). Production of kinetic energy is the only source and dissipation by molecular viscosity is the only sink in the kinetic energy budget. Turbulent, molecular and pressure transports only redistribute energy in the transverse direction, while pressure dilatation (Π) and fluctuating mass flux contributions (M) are negligible for all the cases considered here. Turbulent kinetic energy production and dissipation are shown in figure 4(*b*). With an increase in M_c, energy production decreases and the changes in the dissipation of energy are not as large as those in production. Therefore, the difference in energy levels arises from a reduced level of production at higher convective Mach number. In a temporally evolving mixing layer,

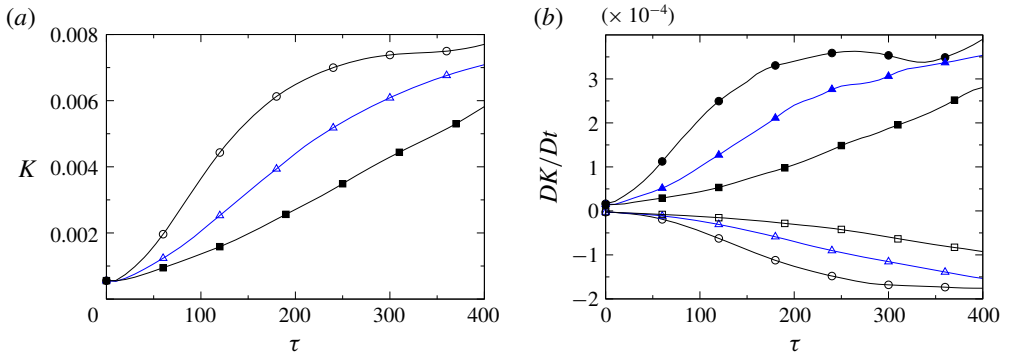

FIGURE 4. (Colour online) (*a*) Evolution of averaged turbulent kinetic energy with time: —○—, $M_c = 0.20$; —△—, $M_c = 0.75$; —■—, $M_c = 1.20$. (*b*) Turbulent kinetic energy production (filled symbols) and dissipation (open symbols): —○—, $M_c = 0.20$; —△—, $M_c = 0.75$; —□—, $M_c = 1.20$. Both turbulent kinetic energy and energy production are lower at higher M_c.

the only non-zero component in the mean velocity gradient tensor is $\mathrm{d}\tilde{u}_1/\mathrm{d}x_2$, and hence the turbulent stress responsible for the production is R_{12} $(= \widetilde{u_1'' u_2''})$ according to (3.6*a*).

A detailed examination of the budgets of R_{12} indicates that the dominant source and sink are respectively production by mean flow gradient $(\mathcal{P}_{12} = R_{22}\,\mathrm{d}\tilde{u}_1/\mathrm{d}x_2)$ and destruction by pressure–strain rate covariance $(\Pi_{12} = \overline{p'(\mathrm{d}u_1''/\mathrm{d}x_2 + \mathrm{d}u_2''/\mathrm{d}x_1)})$. The budget equation may be obtained from equation (3.5) by substituting $i = 1$ and $j = 2$. Viscous dissipation of turbulent shear stress is negligible compared to production and pressure–strain covariance. The time-varying budget terms, in figure 5(*a*), show that the production of turbulent shear stress decreases with increase in Mach number. There exists a balance between shear stress production and pressure–strain correlation during the very early stages of evolution. This regime is characterized by a balance between pressure and inertia effects, according to Bertsch *et al.* (2012), resulting in stabilization of kinetic energy growth. Though the pressure–strain covariance also changes with compressibility, we focus on the stress production because any reduction in source term directly reflects on the shear stress itself. Transverse velocity fluctuations, in the form of R_{22}, are responsible for the production of turbulent shear stress. The dependence is evident from the reduction in transverse velocity fluctuations with M_c, as seen in figure 5(*b*). Transverse fluctuations are also stabilized during the very early stages before they start to grow; the onset of which is delayed by compressibility. Thus, lower R_{12} at higher Mach numbers is due to the reduced intensity of transverse fluctuations as well as the stabilization arising from the balance between the pressure–strain correlation and inertia effects.

The direct production of turbulent fluctuations by the mean flow gradient contributes only to the streamwise fluctuations. In other words, production of R_{22} and R_{33} by the mean velocity gradient is zero since $\tilde{u}_2$ and $\tilde{u}_3$ are zero. The dominant source in the budget of transverse and spanwise fluctuations is pressure–strain rate covariance. In the turbulent energy budget, pressure dilatation (which is the trace of the pressure–strain rate tensor) is negligible in our computations ($\Pi_{kk} = 0$), even when shocklets are observed in the flow field at $M_c = 1.20$. The diagonal components of the pressure–strain rate tensor are not zero, but balance each other such that

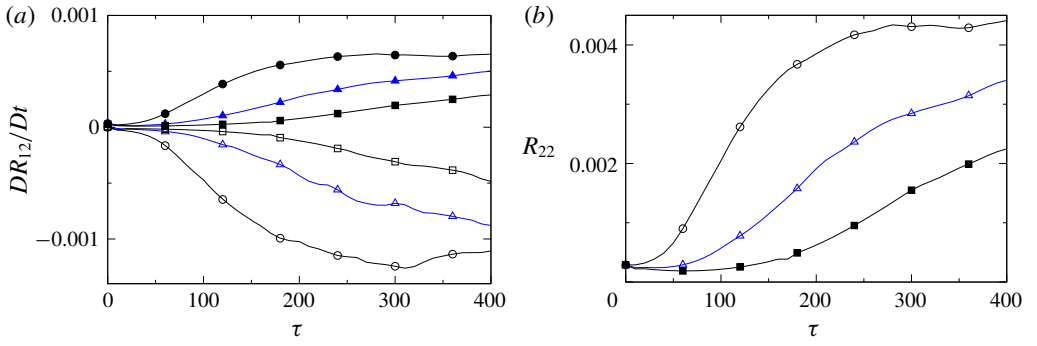

FIGURE 5. (Colour online) (*a*) Production of Reynolds shear stress (filled symbols) and pressure rate of strain correlation, Π_{12} (open symbols) at different Mach numbers; —○—, $M_c = 0.20$; —△—, $M_c = 0.75$; —■—, $M_c = 1.20$. There is a significant decrease in production as M_c increases. (*b*) Evolution of averaged R_{22} for different M_c. The reduced production of R_{12} is due to decreasing levels of transverse fluctuations (R_{22}) with increase in M_c.

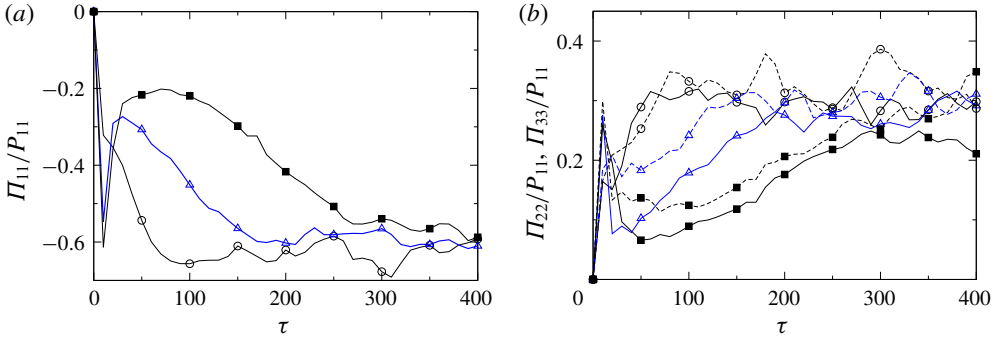

FIGURE 6. (Colour online) Redistribution terms in the budget of turbulent normal stresses: (*a*) Π_{11}; (*b*) ——, Π_{22} and - - -, Π_{33}. The plots are for three different cases: —○—, $M_c = 0.20$; —△—, $M_c = 0.75$; —■—, $M_c = 1.20$.

$\Pi_{11} \approx -(\Pi_{22} + \Pi_{33})$. This is often referred to as the redistribution of energy by pressure–strain rate covariance (Pope 2000). It can be perceived as Π_{11} extracting some amount of energy from streamwise velocity fluctuations and redistributing that to the other two fluctuating velocity components.

The values of diagonal terms in Π_{ij}, averaged in the transverse direction according to (3.4), varies with time, and their evolution is given in figure 6. The individual components of the covariance tensor are normalized by the streamwise fluctuation production ($\mathcal{P}_{11}$), which enables us to compare the efficiency of pressure–strain covariance in redistributing the available energy among different velocity components. Irrespective of Mach number, the redistribution to transverse and spanwise fluctuations are approximately equal, and the turbulence is expected to have an axisymmetric structure. There is no equipartition of energy between transverse fluctuations and internal energy as observed by Lavin *et al.* (2012) for homogeneous shear turbulence, but the energy is almost equally distributed between transverse and streamwise fluctuating components. The magnitudes of diagonal components of pressure–strain

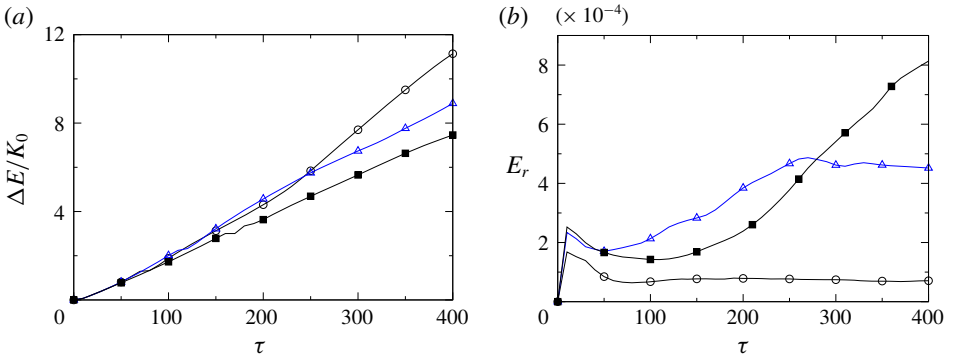

FIGURE 7. (Colour online) (*a*) Change in mean internal energy in the mixing layer with time. (*b*) Evolution of averaged thermodynamic potential energy; —○—, $M_c = 0.20$; —△—, $M_c = 0.75$; —■—, $M_c = 1.20$.

covariance, namely Π_{11}, Π_{22} and Π_{33}, decrease with increasing M_c, especially during the early stages. Therefore it is evident that redistribution is less efficient as compressibility effects become significant.

The evolution of averaged internal energy in the mixing layer is shown in figure 7(*a*). We report the change in mean internal energy from its initial value ($\Delta E = c_v[\tilde{T} - \tilde{T}_0]$), normalized by the initial fluctuation kinetic energy. The internal energy increases with time primarily due to the energy transfer from kinetic energy by viscous dissipation. In compressible turbulent flows, there is energy transfer to the internal mode by dilatational effects, including dilatational dissipation and pressure dilatation in addition to the incompressible viscous dissipation (Lele 1994). Internal energy increases more rapidly for lower M_c, which implies that the dilatational effects are negligible and transfer is mainly through viscous dissipation, which decreases when M_c increases, as seen in figure 4(*b*). However, the thermodynamic potential energy, defined by $E_T = \overline{p'^2}/\gamma\bar{p}$, exhibits different behaviour. Sarkar *et al.* (1991) and Lee & Girimaji (2013) used this quantity to quantify the energy associated with thermodynamic fluctuations. The evolution of average E_T in the shear layer is shown in figure 7(*b*). The potential energy increases with M_c, which implies that even though the energy transfer from kinetic mode to internal mode decreases with compressibility, there is an increase in energy transfer to thermodynamic fluctuations.

Pantano & Sarkar (2002) attributed the lower levels of production to a decrease in pressure–strain term with increasing M_c in their self-similar analysis. They also noted that the decrease in Π_{11} is similar to that in pressure fluctuations with increasing compressibility. The present study shows that the initial evolution of the mixing layer is also characterized by differences in the redistribution of energy by pressure–strain rate covariance, as they are in the self-similar regime. The pressure–strain correlation and root mean square of pressure fluctuations at the centreline for different convective Mach numbers at $\tau = 200$ are shown in figure 8. The quantities are normalized by the incompressible ($M_c = 0.20$) value. There is a direct correlation between redistribution and pressure fluctuations. Pantano & Sarkar (2002) observed similar trends in the self-similar regime. Thus, the reduced redistribution during the transient evolution is caused by the suppression of pressure fluctuations by compressibility. Apart from the variations in redistribution, we also observe that there is a stabilization of turbulent

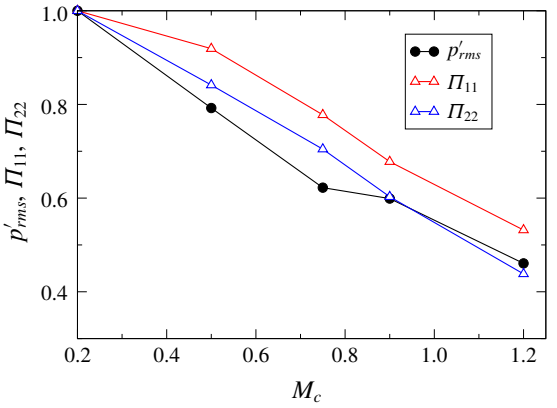

FIGURE 8. (Colour online) Pressure–strain correlation and pressure fluctuation at different M_c, normalized by the incompressible value.

shear stress growth due to the balance between stress production and pressure–strain correlation when compressibility effects are significant.

3.3. *Topological considerations*

Turbulent statistics can be influenced by variations in topology. We use the Q-criterion to classify the topology of the flow into two distinct categories (Hunt *et al.* 1988). The second invariant (Q) of the velocity gradient tensor is given by

$$Q = -\tfrac{1}{2}(\mathcal{S}_{ij}\mathcal{S}_{ij} - \Omega_{ij}\Omega_{ij}). \tag{3.9}$$

In the above, $\mathcal{S}_{ij} = [\nabla u'' + \nabla u''^{\mathrm{T}}]/2$ and $\Omega_{ij} = [\nabla u'' - \nabla u''^{\mathrm{T}}]/2$ are respectively the symmetric and anti-symmetric parts of the deviatoric strain rate tensor, $\nabla u'' = u''_{i,j} - u''_{k,k}\delta_{ij}/3$. The criterion, originally developed for incompressible flows, is valid for compressible flows only when the invariant is obtained for deviatoric part of velocity gradient tensor (Kolár 2009). Local flow structure is classified according to the numerical value of Q. According to the criterion, a positive value of Q indicates that the flow is locally vortex-dominated and negative values indicate strain-dominated regions. In the present work, the topology is determined using the fluctuating quantities, since for the mean field Q turns out to be zero. In this section, we analyse various turbulent statistics conditioned on the value of $\bar{Q} = Q/Q_{rms}$ to study how changes in local flow topology due to compressibility manifests on turbulent statistics. An average in the homogeneous plane is used for the root mean square (r.m.s.) calculation. The sample used to calculate the conditional statistics is the region $-2\delta_\theta \leqslant x_2 \leqslant 2\delta_\theta$, which constitutes the turbulent core of the mixing layer. Extreme events, $|\bar{Q}| \gg 1$, are not discussed here. Various quantities from each spatial location are put into different bins based on the local value of $\bar{Q}$ and conditional averages for different $\bar{Q}$ are obtained by averaging the data in respective bins.

Distribution of turbulence among different flow topologies is given by the turbulent kinetic energy conditioned on $\bar{Q}$, as in figure 9. The figure shows the variation of the conditional mean of $u''_k u''_k$, normalized by $2K(y)$, with $\bar{Q}$. For negative values of $\bar{Q}$, the conditioned turbulent kinetic energy is higher than the overall turbulent kinetic energy. There is a sharp drop in the conditional mean as $\bar{Q}$ increases from zero.

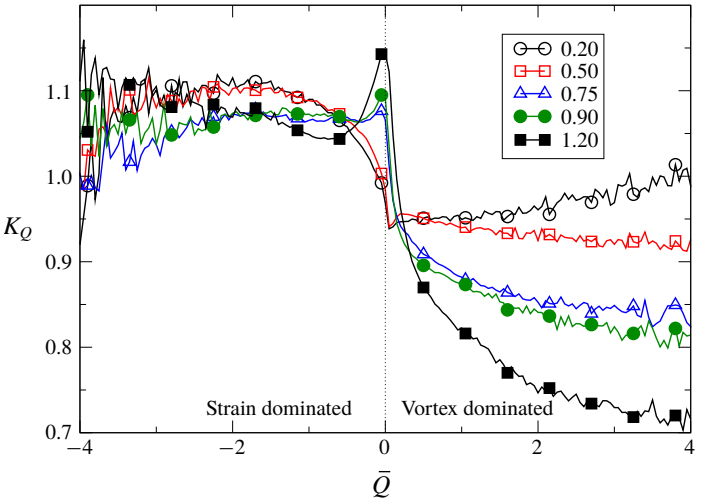

FIGURE 9. (Colour online) Conditional mean of turbulent kinetic energy, $K_Q = \langle u_k'' u_k'' | \bar{Q} \rangle / 2K$, representing spatial distribution of turbulent energy among different topologies, for different cases at $\tau = 300$.

This implies that the turbulent fluctuations are more intense in shear-dominated regions, and their relative contribution towards overall kinetic energy is higher. The conditional mean remains nearly constant in the strain-dominated regions, and they are less influenced by changes in M_c. In vortex-dominated regions, the normalized conditional kinetic energy has values less than unity and decreases as $\bar{Q}$ increases in the compressible flow regime (large M_c). As M_c increases, the conditional mean for a given $\bar{Q}$ decreases in vortex-dominated regions. At the highest Mach number considered, the conditional mean is only approximately 0.60 times the turbulent kinetic energy in vortex-dominated regions. Thus, vortex-dominated regions have less turbulence intensity, and in the absence of these flow structures, the overall turbulent kinetic energy would have been higher owing to higher intensities in strain-dominated regions. For the range of turbulent Mach numbers in our study, it is safe to conclude that there is a preferential distribution of turbulent kinetic energy in regions of negative $\bar{Q}$.

We have already observed in § 3.2 that differences in turbulent kinetic energy with compressibility arise from reduced levels of production. Ma & Xiao (2016) showed that the turbulent kinetic energy production is more in strain-dominated regions, in the case of homogeneous turbulent shear flows. In our simulations, mixing layer evolves in such a way that turbulent energy production is due to Reynolds shear stress, R_{12}, as discussed earlier. So any influence of local flow structure on energy production must be evident from a conditioned average of $\rho u_1'' u_2''$. The conditional mean of turbulent shear stress, normalized by $\bar{\rho}(y) R_{12}(y)$ is shown in figure 10. There is a stronger co-variance of fluctuating streamwise and transverse velocities in regions dominated by strain which means those regions produce more fluctuating energy than vortex-dominated regions. For the nearly incompressible case (M2), the conditional mean gradually decreases as $\bar{Q}$ increases from negative values to positive values. For moderate M_c (M5 and M7), the conditional mean is nearly constant for $\bar{Q} < 0$, peaks at $\bar{Q} = 0$ and monotonically decreases beyond that. For the larger Mach numbers, the conditional turbulent stress increases with $\bar{Q}$ in the strain-dominated regions,

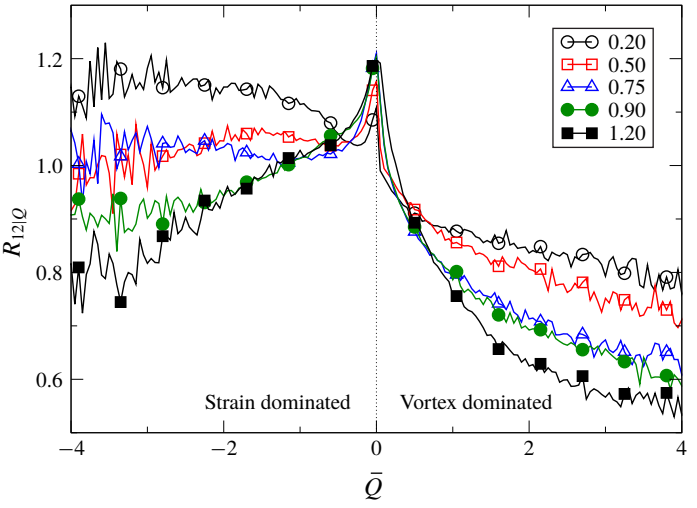

FIGURE 10. (Colour online) Turbulent shear stress conditioned on the value of $\bar{Q}$, $R_{12|Q} = \langle \rho u_1'' u_2'' | \bar{Q} \rangle / \bar{\rho} R_{12}$, for different convective Mach numbers at $\tau = 300$.

reaches a maximum at $\bar{Q} = 0$ and decreases as $\bar{Q}$ increases in the vortex-dominated regions. Most of the production happens at small negative values of $\bar{Q}$. However, at all M_c, the conditional mean has higher values in strain-dominated regions than that in vortex-dominated regions. Similar to turbulent kinetic energy, the shear stress also decreases as M_c increases for a given positive value of $\bar{Q}$. Thus structures which are strongly dominated by vortex-like motions are less efficient in extracting energy from mean flow to turbulence. The spatial distribution of production explains the higher turbulence intensity in strain-dominated regions. The observation relating energy production and the fluctuating velocity gradient in compressible mixing layers was hitherto unknown.

The Reynolds shear stress, R_{12}, represents turbulent transport of fluctuating streamwise momentum ($\rho u_1''$) by transverse fluctuations (u_2''). Conditioned statistics in figure 10 imply that vortex-dominated regions do not transport as much fluctuating momentum as strain-dominated regions do. A closer look at flow structure in regions of strong positive $\bar{Q}$ makes apparent how local flow topology affects turbulent stress. Figure 11 shows the streamline pattern around a tube-like structure with $\bar{Q} = 1.1$ for $M_c = 0.75$ at $\tau = 200$. Streamlines are coloured by $sgn(u_1'' u_2'')$, solid red for positive values and dashed blue for negative values. The streamlines are helical near the vortex-dominated region, swirling around the tube-like structure. Such helical streamlines are characteristic of vortex-dominated regions. Moving along the helical streamline, the product $u_1'' u_2''$ alternates between positive and negative values. Therefore, any net positive contributions to R_{12} from these regions are small and turbulent transport of fluctuating momentum is less compared to regions where such helical streamlines are absent. This kind of flow pattern is more likely to diminish turbulent production when these streamlines are aligned with their axes along the streamwise direction. Helical streamlines with their axes inclined away from the streamwise direction may contribute significantly to the turbulent shear stress and thus the energy production. A better understanding of the inclination of such streamlines is given by an in-depth analysis of the structure of the vortex field in § 3.4. Although the

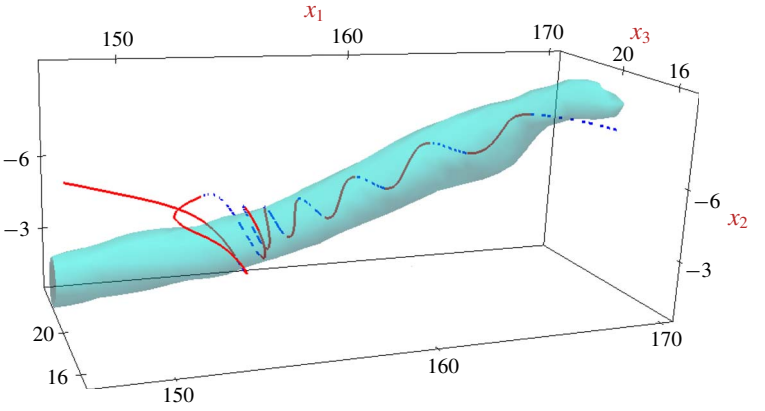

FIGURE 11. (Colour online) Streamlines around a vortex-dominated tube-like structure in the flow. The structure is contour of $\bar{Q} = 1.1$ from an instantaneous snapshot of the flow field at $\tau = 200$ for $M_c = 0.75$. Solid parts of the streamline indicate that $u_1'' u_2''$ is positive in those regions and dashed lines indicate that the product is negative.

streamline pattern shown in figure 11 is instantaneous, we have observed several such patterns in the flow field for all the cases, and all helical streamlines are found in the regions of positive $\bar{Q}$. Not all regions of positive $\bar{Q}$, however, have a helical streamline pattern.

Turbulent kinetic energy production in simple shear flows is linked to redistribution effects of the pressure–strain correlation tensor (Π_{ij}), as described in § 3.2. Turbulent stress, responsible for energy production in mixing layers, depends on transverse velocity fluctuations, which are produced by redistribution of energy by diagonal components of Π_{ij}. We observed that compressibility reduces redistribution by Π_{ij}. Therefore, it is imperative to investigate the effects of local flow topology on energy redistribution. Redistribution of kinetic energy depends on the local flow structure, as shown in figure 12, where we plot conditional average $\Pi_{11|Q} = \langle -p' \partial u_1''/\partial x_1 | \bar{Q} \rangle / (K \Delta U/\delta_\theta)$ against $\bar{Q}$. The quantity on the vertical axis represents the rate of energy extraction from streamwise fluctuations by pressure–strain covariance, which then is redistributed between the transverse and spanwise fluctuating components. The conditional mean is minimum for $\bar{Q} = 0$, but increases as the topology become either strain dominated or vortex dominated. However, the strain-dominated regions have higher values for the conditional mean than vortex-dominated regions and the difference increases with M_c. Thus strain-dominated regions, where $\bar{Q} < 0$, are significantly more effective in transferring energy from streamwise fluctuations to the other directions. Redistribution by pressure–strain in vortex-dominated regions is comparatively less, especially at higher Mach numbers. These differences contribute to the preferential distribution of production and kinetic energy discussed above.

The turbulent kinetic energy has a dependence on local flow structure, which is due to a preferential distribution of energy production and redistribution. However, the preferential distribution of kinetic energy and production exist at all Mach numbers in our study. Therefore it is difficult to explain reduced turbulence levels at higher Mach numbers based on conditional statistics alone. However, the probability density function (PDF) of $\bar{Q}$ shows that the flow topology is changed by compressibility.

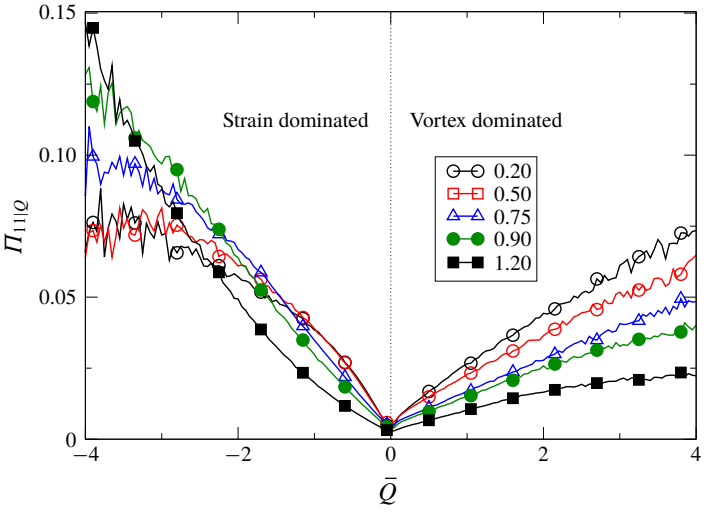

FIGURE 12. (Colour online) Conditional average of pressure–strain covariance $\Pi_{11|Q} = \langle -p'(\partial u_1''/\partial x_1)|\bar{Q}\rangle/(K\Delta U/\delta_\theta)$ in the turbulent mixing layer at different convective Mach numbers.

Figure 13 compares the PDF of $\bar{Q}$ for $M_c = 0.20$ and 1.20. At higher convective Mach numbers, the probability of the occurrence of positive values of $\bar{Q}$ is higher than that in lower Mach number cases. The fraction of the shear layer which has a locally vortex-dominated topology, calculated by the area under PDF curve for $\bar{Q}$, for different cases is listed in table 2. At any given instant of time or mixing-layer width, the fraction of the shear layer with vortex-dominated structures increases with convective Mach number. Nevertheless, strain-dominated regions are more prominent than vortex-dominated regions at all Mach numbers, according to the values in table 2. The lower turbulent kinetic energy at higher Mach numbers can thus be attributed to the higher fraction of vortex-dominated regions which are less efficient in kinetic energy production and redistribution. The differences in topology tend to even out at later times and any differences in turbulent statistics due to differences in local flow structure are expected to be small during the late time and self-similar evolution of the mixing layer. In addition to the pressure dilatation effects, a vortex-dominated topology also contributes towards lower levels of turbulence as convective Mach number increases.

3.4. *Vortex vectors*

In § 3.3, the Q-criterion was used to identify the vortex-dominated regions and the reported statistics were conditioned on the value of Q, a scalar. Vortex identification using the Q-criterion lacks information on the direction of rotation, or on the orientation of these vortex-dominated structures. Recently, Tian *et al.* (2018) (from now on TGDL18) defined a quantity called the vortex vector which not only identifies vortex-dominated regions but also gives the direction of rotation of the fluid element locally. In this section, we apply their definition of the vortex vector to our DNS data to analyse the effects of compressibility.

At any point in the flow field, TGDL18 defines a local rotation axis relative to which fluid has rotational motion in the plane orthogonal to the axis. Let us denote

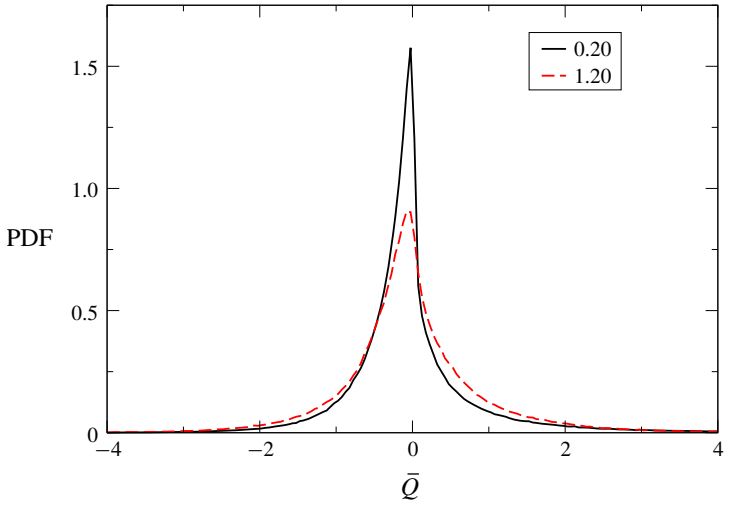

FIGURE 13. (Colour online) Probability density function of $\bar{Q}$ in the turbulent shear layer for $M_c = 0.20$ and 1.20 at $\tau = 300$. Data correspond to $-2\delta_\theta \leqslant x_2 \leqslant 2\delta_\theta$.

τ	M2	M5	M7	M9	M12
200	34	37	41	42	46
250	36	37	39	40	44
300	36	37	38	38	43
350	36	37	38	38	42
$\delta_\theta/\delta_{\theta_0}$	M2	M5	M7	M9	M12
3	40	40	44	45	45
5	36	37	38	39	41
7	36	37	38	38	40

TABLE 2. Percentage of vortex-dominated regions in the turbulent shear layer, estimated from the probability density function of $\bar{Q}$, for different cases. The changes in topology with time (top) and growth of the mixing-layer thickness (bottom) for different cases show that higher M_c has more vortex-dominated regions in the flow field.

this local rotation axis by z, and let xy be the plane orthogonal to this axis. Then xyz is an orthogonal coordinate system which varies from point to point due to the change in orientation of the local rotation axis. By definition, there is no rotational motion of the fluid element in any plane other than xy. This requires that the local velocity field $\boldsymbol{V} = (u, v, w)$ in the local orthogonal coordinate system satisfies $\partial u/\partial z = 0$ and $\partial v/\partial z = 0$. These are necessary and sufficient conditions for z to be the local rotation axis. The unit vector along z in the general reference frame is given by $\boldsymbol{r} = r_1\hat{e}_1 + r_2\hat{e}_2 + r_3\hat{e}_3$, where $\hat{e}_1$, $\hat{e}_2$ and $\hat{e}_3$ are unit vectors in the general reference frame along the x_1, x_2 and x_3 directions respectively. The vector $\boldsymbol{r}$ at each point is obtained by solving the following equations,

$$r_1^2 + r_2^2 + r_3^2 = 1, \tag{3.10a}$$

$$\frac{\partial u}{\partial z} = 0, \tag{3.10b}$$

$$\frac{\partial v}{\partial z} = 0, \tag{3.10c}$$

where the velocity gradients in the local coordinate system are given by a transformation from the original reference frame. The velocity gradient tensor in the xyz frame, denoted by $\nabla \boldsymbol{V}$, is related to that in the original reference frame, $\nabla \boldsymbol{u}$, as

$$\nabla \boldsymbol{V} = \boldsymbol{A} \nabla \boldsymbol{u} \boldsymbol{A}^{-1}, \tag{3.11}$$

where $\boldsymbol{A}$ is the orthogonal transformation matrix. The transformation matrix is a function of the local rotation axis and is given by

$$\boldsymbol{A} = \begin{bmatrix} \dfrac{r_2^2 + r_3^2 + r_3}{1 + r_3} & -\dfrac{r_1 r_2}{1 + r_3} & -r_1 \\ -\dfrac{r_1 r_2}{1 + r_3} & \dfrac{r_1^2 + r_3^2 + r_3}{1 + r_3} & -r_2 \\ r_1 & r_2 & r_3 \end{bmatrix}. \tag{3.12}$$

Since $\nabla \boldsymbol{u}$ is known, equation (3.10) becomes a system of nonlinear equations with r_1, r_2 and r_3 as unknowns. This set of equations are solved using the Newton–Raphson method, with local vorticity direction as an initial guess.

The conditions imposed to define the local rotation axis only imply that there is no rotation around the other axes in the orthogonal reference frame, but they do not mean that the fluid element is rotating about the z-axis. The rotation of the fluid also needs to be quantified. The fluid element is deemed to be rotational depending on the values of α and β, which are defined as follows,

$$\alpha = \frac{1}{2} \sqrt{\left(\frac{\partial u}{\partial x} - \frac{\partial v}{\partial y} \right)^2 + \left(\frac{\partial v}{\partial x} + \frac{\partial u}{\partial y} \right)^2}, \tag{3.13}$$

$$\beta = \frac{1}{2} \left(\frac{\partial v}{\partial x} - \frac{\partial u}{\partial y} \right). \tag{3.14}$$

The fluid element has a rotational deformation only when $\beta^2 > \alpha^2$ and then the strength of rotation is defined as

$$R_z = \begin{cases} 2(\beta - \alpha), & \beta^2 - \alpha^2 > 0, \beta > 0, \\ 2(\beta + \alpha), & \beta^2 - \alpha^2 > 0, \beta < 0, \\ 0, & \beta^2 - \alpha^2 \leqslant 0. \end{cases} \tag{3.15}$$

With the local rotation axis and strength of rotation known, the vortex vector at any point in the flow field is given by

$$\boldsymbol{R} = R_z \boldsymbol{r}. \tag{3.16}$$

The vortex vector represents the magnitude and direction of the local fluid rotation and a connected region where $\boldsymbol{R} \neq 0$ is a vortex. Rigorous mathematical proofs for the definitions can be found in Liu *et al.* (2018).

We employ this method to find the vortex vectors and identify vortices in the turbulent mixing layer at different M_c. According to TGDL18, iso-surfaces of the

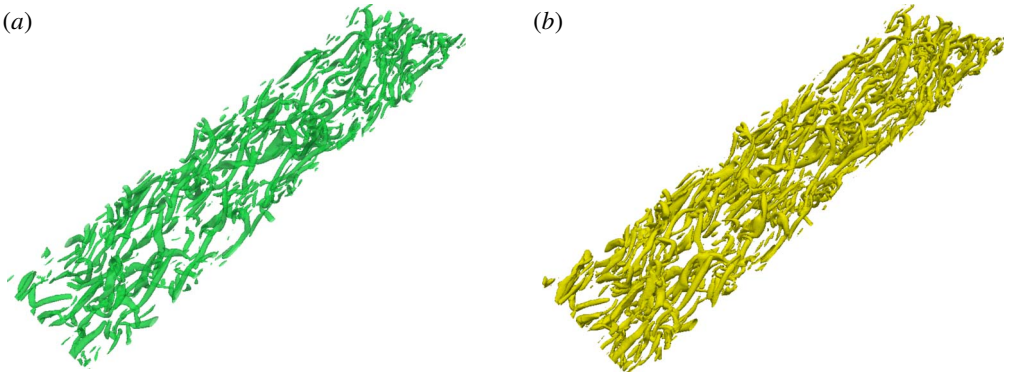

FIGURE 14. (Colour online) Visualization of vortical structures in a turbulent mixing layer using the Q-criterion and vortex vector. The figures are instantaneous snapshots for $M_c = 0.75$ at $\tau = 200$. (*a*) Contours of $\hat{Q} = 0.07$, where $\hat{Q}$ is the value of Q normalized by $(\Delta U/\delta_{\theta_0})^2$. (*b*) Iso-surfaces of normalized $|\boldsymbol{R}| = 0.05$.

vortex vector magnitude can be used to visualize the vortices in the flow. The vortex vector is normalized by $\Delta U/\delta_{\theta_0}$ in this study. For the conditional statistical analysis in the previous section, the Q-criterion was used to identify vortex-dominated regions. In figure 14, we compare the visualization of vortices in the flow field using the Q-criterion and vortex vector. Figure 14(*a*) shows contours of $\hat{Q} = 0.07$ and figure 14(*b*) shows the iso-surfaces of $|\boldsymbol{R}| = 0.05$ for $M_c = 0.75$ at time $\tau = 200$. The iso-surfaces in the latter are qualitatively similar to the contours of $\hat{Q}$, albeit there are differences in small-scale structure. The large-scale structures in either visualization match very well. The figures may exactly match each other if the contour values are chosen appropriately. Since the relation between the strength of rotation and the Q value is unknown at this point of time, it is not possible to predict the value of $\hat{Q}$ which exactly matches the iso-surfaces for a given value of rotation strength. Nevertheless, it is safe to assume that the vortex-dominated regions identified by the Q-criterion are regions of finite rotation strength.

Vortex vector also gives the direction of rotation, which the Q-criterion does not. The vector is directed along the local rotational axis defined earlier. Figure 15(*a*) shows the vortex vectors on a hairpin vortex core, identified using rotation strength, in the flow field. The hairpin vortex is one of several similar structures in figure 14(*b*) and is isolated by magnifying the same figure. The vortex vectors show the direction of rotation at each point, and their length is proportional to the magnitude of the vortex vector. These vortex vectors align with the identified vortex core structure and indicate the direction of local rotation axis at each point. The fluid element rotates about the vortex vector in a plane perpendicular to it. In fluid mechanics, the lines formed by the vorticity vector is referred to as vortex lines. However, TGDL18 define vortex lines as lines whose tangent at any point is along the vortex vector, not the vorticity vector, at that point. A few vortex lines in the neighbourhood of the same hairpin vortex structure are shown in figure 15(*b*). These vortex lines also capture the shape of the hairpin structure as good as the iso-surface of rotation strength. The lines are coloured by the local rotation strength, which helps in finding out where the rotation is strong or weak. With the Q-criterion or other vortex identification techniques, it is not possible to quantify the strength of local rotation. For example,

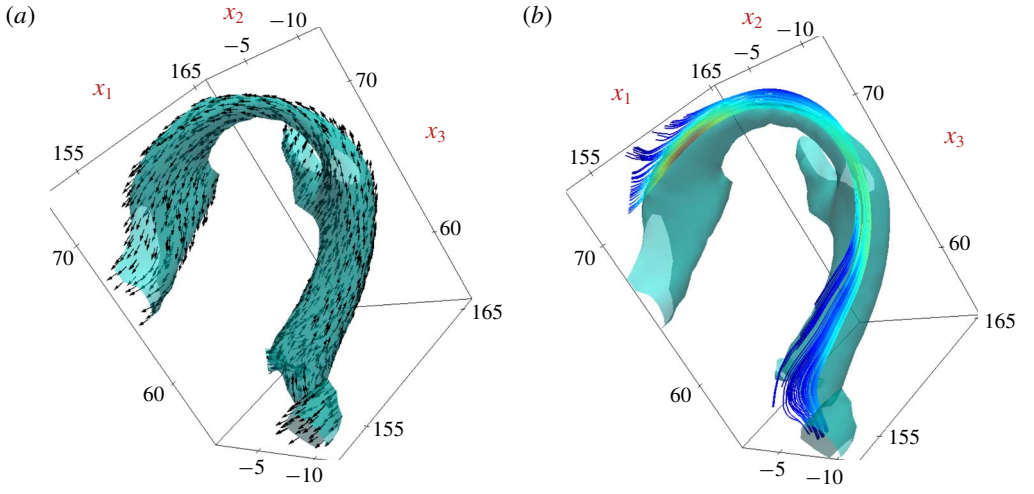

FIGURE 15. (Colour online) Vortex vectors and vortex lines on a hairpin-like structure, identified using iso-surface of vortex strength ($|\boldsymbol{R}| = 0.05$), in a turbulent mixing layer for $M_c = 0.75$ at $\tau = 200$. (*a*) Vortex vectors on the vortical structure. (*b*) Vortex lines passing through the vortical structure coloured by the local strength of rotation.

Q, defined by equation (3.9), is not a measure of rotation itself. It only indicates whether vorticity or strain rate is dominant. Vortex vector, on the other hand, describes both the strength and direction of local fluid rotation.

In § 3.3, we discussed how the turbulent statistics are different in regions with vortical structures compared to those in other regions. It was found that turbulent kinetic energy production is lower in regions of positive Q, and the reduction was attributed to the helical streamline patterns in the vortex-dominated regions (refer to figure 11). Changes in turbulent shear stress (R_{12}), which are responsible for energy production, are mirrored by those in the inclination of these vortex lines with respect to the streamwise direction as explained below. Let us consider a helical streamline pattern with the axis of helix along the streamwise direction as in figure 16(*a*). Along the streamline, the transverse velocity changes from positive to zero to negative and *vice versa*. Assuming that the streamwise velocity fluctuations do not change significantly in the neighbourhood of this streamline pattern, the product of the two fluctuating velocity components also shows similar behaviour. Hence the average of this product, which is the correlation $\overline{u_1'' u_2''}$, is not expected to have a very large magnitude. However, this behaviour changes when the axis of the helix becomes inclined to the streamwise direction, as shown in 16(*b*). When θ, the angle between the axis of the helix and streamwise direction, takes large positive or negative values, the transverse velocity along the streamline does not alternate between positive and negative values. Instead, it remains biased towards either positive or negative u_2''. For example, the helical streamline in figure 16(*b*) has a positive transverse velocity at almost every point of the streamline. In such a scenario, the magnitude of the correlation $\overline{u_1'' u_2''}$ can be significantly larger than when the helix axis is along the streamwise direction. The relationship between velocity correlation and streamwise inclination is described in appendix B. Therefore, the reduced turbulent production at higher M_c in vortex-dominated regions can be explained by quantifying the inclination of helical streamlines with the streamwise direction.

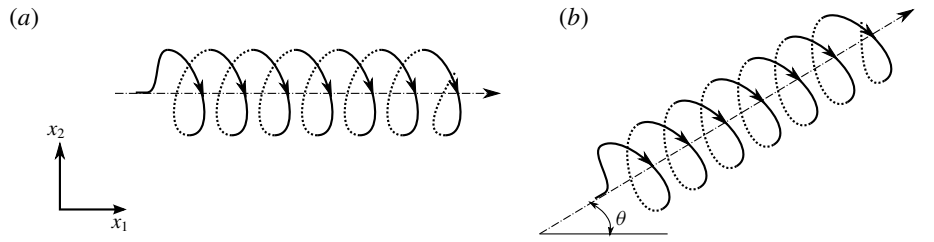

FIGURE 16. (*a*) Schematic diagram of a helical streamline with axis of helix along streamwise direction. Correlation $\overline{u_1''u_2''}$ is very small in this case. (*b*) Streamline with axis at an angle θ to the streamwise direction. Since u_2'' at most points along the streamline is positive, $\overline{u_1''u_2''}$ is significantly large. For details refer to appendix B.

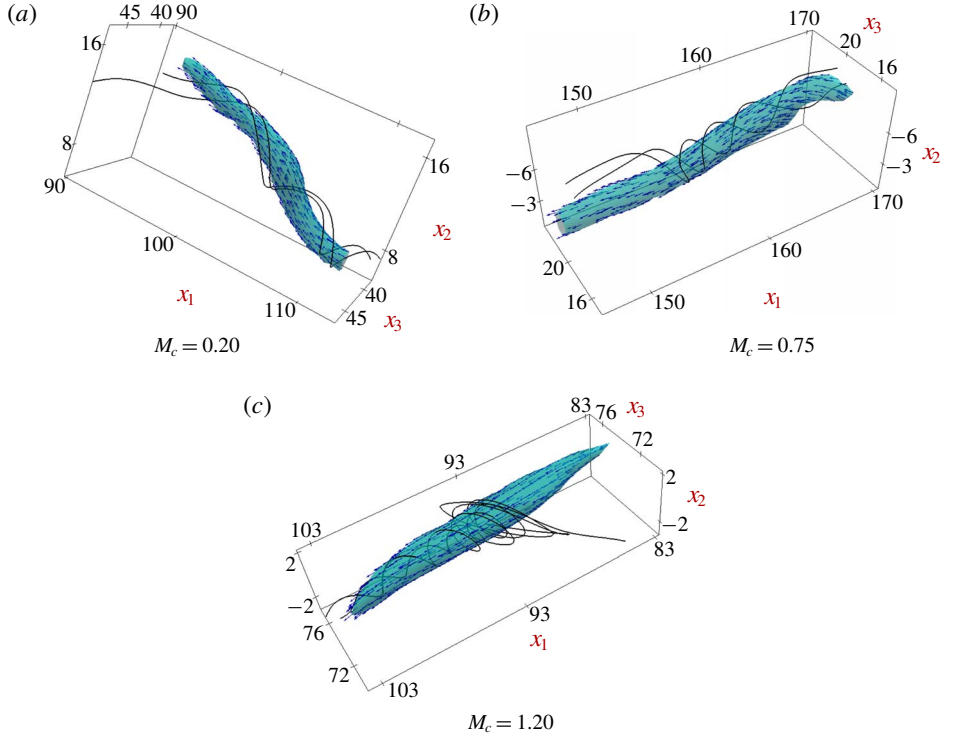

FIGURE 17. (Colour online) Vortical structures in the turbulent mixing-layer flow field identified using the Q-criterion and the streamline pattern around the vortical structures for different cases. The streamlines are generated by seeding random points on the surface of the tube-like structures. The arrows are vortex vectors which are along the axis of the helical streamlines.

The vortex vector can, by evidence, not only identify but also describe the orientation of the vortical structures in the flow field. Vortex vector is oriented along the local rotation axis defined earlier, which also coincides with the axis of any helical streamlines present in the region. Vortex-dominated regions, identified using the Q-criterion, in the flow field for three different Mach numbers are shown in figure 17. The streamlines around vortex-dominated regions have a helical pattern

with axis along the filament-like structures. The streamlines are generated by seeding at points very close to the iso-surfaces. At higher M_c, the streamlines spiral more than that at lower Mach numbers. Vortex vectors are also shown in the figure and are parallel to the axis of the helical streamline shown. Thus the orientation of helical streamlines in the flow field can be quantified using vortex vectors.

3.5. *Structure of vortex field*

In the turbulent mixing layer, there are several regions where helical streamlines are present, especially in vortex-dominated regions. The orientation of such streamlines can be revealed by a statistical analysis of the vortex vector. Similar analyses of vorticity fields have been performed for turbulent channel flows by Moin & Kim (1985) and for incompressible homogeneous shear turbulence by Rogers & Moin (1987). The orientation of vortex vectors with respect to the streamwise direction is of particular interest due to the reasons discussed earlier. The angle between the vortex vector and streamwise direction can be calculated from the scalar product of the vortex vector and the unit vector along the streamwise direction. Similarly, the orientations with respect to the transverse and spanwise directions are also given by scalar products. Thus the orientation of the vortex vector is defined by

$$\cos\theta = \boldsymbol{R}\cdot\hat{e}_1/|\boldsymbol{R}|, \tag{3.17}$$

$$\cos\phi = \boldsymbol{R}\cdot\hat{e}_2/|\boldsymbol{R}|, \tag{3.18}$$

$$\cos\psi = \boldsymbol{R}\cdot\hat{e}_3/|\boldsymbol{R}|, \tag{3.19}$$

where θ, ϕ and ψ are respectively the angles made by the vortex vector with the positive streamwise, transverse and spanwise directions. A statistical analysis based on the PDF or joint probability density functions (JPDF) of these angles in the turbulent mixing layer provides information on the orientation of the vortex vectors. The JPDFs for different M_c enable us to study how compressibility changes the vortical structures in mixing layers. We analyse the joint probability density function of the cosine of the angles, pairing them with each other, to understand how the vortex vectors are oriented when they are projected onto spanwise, streamwise and transverse planes. Only the points which are in the core of the turbulent mixing layer, that is $-2\delta_\theta \leqslant x_2 \leqslant 2\delta_\theta$, are used for the analysis. Points which are locally irrotational are omitted because the vortex vector has zero magnitude at those points. For the analysis, the cosines of the angles, instead of the angles themselves, are used.

For mixing layers, the joint probability density function for $\cos\theta$ and $\cos\phi$ is more important than the other two in understanding the relation between vortex vector orientation and turbulence production. The JPDF, denoted henceforth by $P(\theta, \phi)$, reflects the orientation of vortex vectors projected onto a spanwise plane. A JPDF analysis of vorticity components in turbulent boundary layers was performed by Ong & Wallace (1998), where they observed significant changes in the JPDFs of vorticity components at different transverse locations. Moin & Kim (1985) also observed that the structure of the vorticity field depends on the distance from the wall in turbulent channel flows. Therefore, a similar study is undertaken here to see if there is any dependence of vortex vector orientations on the transverse location by examining the statistics at different x_2. Figure 18 shows $P(\theta, \phi)$ at three transverse locations, viz $x_2 = 0$, δ_θ, $2\delta_\theta$, for $M_c = 0.20$. These plots correspond to the non-dimensional time $\tau = 200$. The figures show contours of $P(\theta, \phi)$ and the contour levels, indicated in 18(*c*), are the same for all the three figures. The large values of $P(\theta, \phi)$ occur in quadrants II and IV of the $\cos\theta - \cos\phi$ plane with peaks around $\cos\theta \approx \pm 0.8$ at all

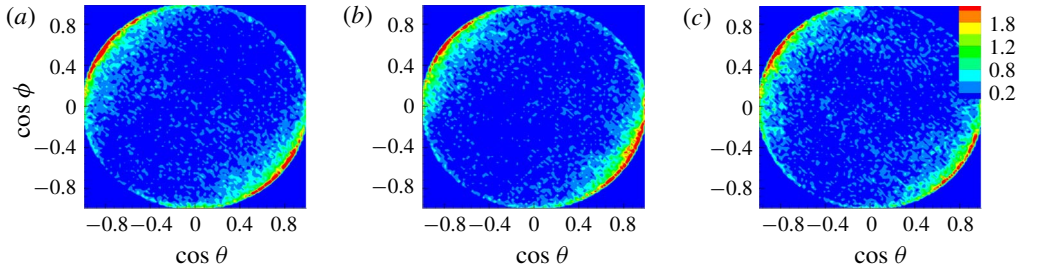

FIGURE 18. (Colour online) The JPDFs of $\cos\theta$ and $\cos\phi$ at different transverse locations for $M_c = 0.20$ at $\tau = 200$. (*a*) $x_2 = 0$, (*b*) $x_2 = \delta_\theta$ and (*c*) $x_2 = 2\delta_\theta$.

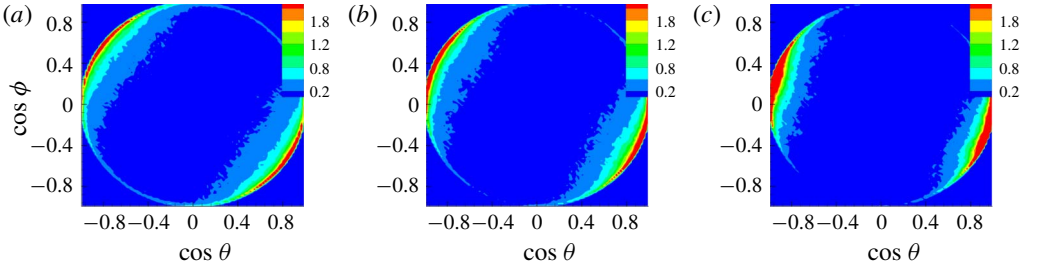

FIGURE 19. (Colour online) The JPDFs, $P(\theta, \phi)$, for different Mach numbers at $\tau = 200$ for vortex vectors in the region $-2\delta_\theta \leqslant x_2 \leqslant 2\delta_\theta$. (*a*) $M_c = 0.50$, (*b*) $M_c = 0.90$, (*c*) $M_c = 1.20$.

three transverse locations. This implies that the orientation of vortex vectors does not change significantly from one transverse location to another. Vortex vector orientations remain independent of the transverse location at other Mach numbers studied. For further analysis and comparison across different convective Mach numbers, all the points which are in the turbulent core ($-2\delta_\theta \leqslant x_2 \leqslant 2\delta_\theta$) are considered together as a single set of data. The JPDF of these angles at different M_c is shown in figure 19. Only three sets of results, corresponding to $M_c = 0.50$, 0.90 and 1.20, are presented here. The JPDFs for the nearly incompressible case are very similar to that for $M_c = 0.50$. The other set of results not presented here corresponds to $M_c = 0.75$ for which the distributions closely resemble those for $M_c = 0.90$. At all three Mach numbers, the high probability regions, indicated by red colour, falls in the second and fourth quadrants of the Cartesian plane defined by $\cos\theta$ and $\cos\phi$ as axes.

The vector $\cos\theta\hat{e}_1 + \cos\phi\hat{e}_2$ is the projection of the unit vector along $\boldsymbol{R}$ onto the spanwise plane. The angle between the projection and coordinate axes x_1 and x_2 are, respectively,

$$\cos\theta_{2D} = \cos\theta/\sqrt{\cos^2\theta + \cos^2\phi}, \tag{3.20}$$

$$\cos\phi_{2D} = \cos\phi/\sqrt{\cos^2\theta + \cos^2\phi}. \tag{3.21}$$

These angles are not independent of each other and are related, as schematically shown in figure 20(*a*). The JPDFs of the direction cosines of the projected vector reveal the most probable orientations of the vortex vector on the spanwise plane. Non-zero values of JPDFs lie on the unit circle $\cos^2\theta_{2D} + \cos^2\phi_{2D} = 1$. The peaks occur at approximately the same orientations as they occur in figure 19 since the

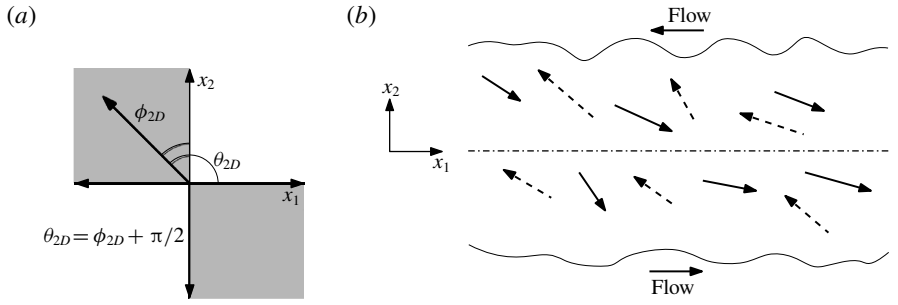

FIGURE 20. (*a*) Schematic diagram showing relation between the cosines for vectors projected onto spanwise plane. Shaded regions represent the more probable orientations of vortex vectors in terms of their direction cosines. (*b*) A schematic of projections of vectors which are more likely to occur in the mixing layer. Solid and dashed arrows correspond to the shaded quadrants IV and II respectively in the figure on the left.

likely orientations of three-dimensional vectors lie close to the unit circle described by $\cos^2\theta + \cos^2\phi = 1$. Hence the high probability regions fall in quadrants II and IV of the Cartesian grid defined by the cosines of the two-dimensional angles. However, since θ_{2D} and ϕ_{2D} are not independent, these quadrants correspond to $\pi/2 \leqslant \theta \leqslant \pi$, $0 \leqslant \phi \leqslant \pi/2$ and $3\pi/2 \leqslant \theta \leqslant 2\pi$, $\pi \leqslant \phi \leqslant 3\pi/2$. The orientation of the projected vectors may be uniquely defined by either θ_{2D} or ϕ_{2D}. The high probability regions fall in the shaded quadrants of figure 20(*a*), and the projection of vortex vectors on the spanwise plane is parallel to the position vectors of points in these quadrants of the x_1–x_2 Cartesian plane.

The mixing layer is set up in such a way that the free-stream velocity is negative for positive x_2 and positive for negative x_2. Schematic diagrams of a few highly probable orientations of the vortex vector projections in the flow field are shown in figure 20(*b*). The solid and dashed arrows correspond to position vectors of points in quadrants II and IV, respectively, as discussed earlier. In the upper stream ($x_2 > 0$), the solid arrows direct towards the centreline while dashed arrows point towards the free stream and *vice versa* in the lower stream. Thus the high probability orientations are, (i) either inclined away from the direction of averaged streamwise velocity and towards the edge of the shear layer (ii) or opposing the free-stream velocity but slightly inclined in such a way that the vectors point towards the centre of the shear layer. Spanwise projection of most probable orientation of the vortex vector can be found using $P(\theta_{2D}, \phi_{2D})$. A similar analysis was used by Ong & Wallace (1998) to find projections of vorticity filaments contributing most to the vorticity covariance in turbulent boundary layers. There are two most probable orientations for the projections which are given by the maximum of JPDF in quadrants II and IV. Using θ_{2D} corresponding to the peak in $P(\theta_{2D}, \phi_{2D})$ at different transverse locations, line segments can be created locally for different x_2. These line segments, with slope $\tan\theta_{2D}$ on the x_3 plane, can be joined together to obtain the projection of the most probable vortex vector orientation on the spanwise plane. This line segment can also be representative of the projection of the most probable vortex structure in the flow field. The reconstructed vortex vector orientations for different M_c at $\tau = 100$ and 300 are shown in figure 21. The most probable orientation of the vortex vector is nearly the same for the lower Mach numbers at $\tau = 100$. As M_c increases, the most likely orientation becomes closer to that of the streamwise direction. For $M_c = 1.20$, vortex

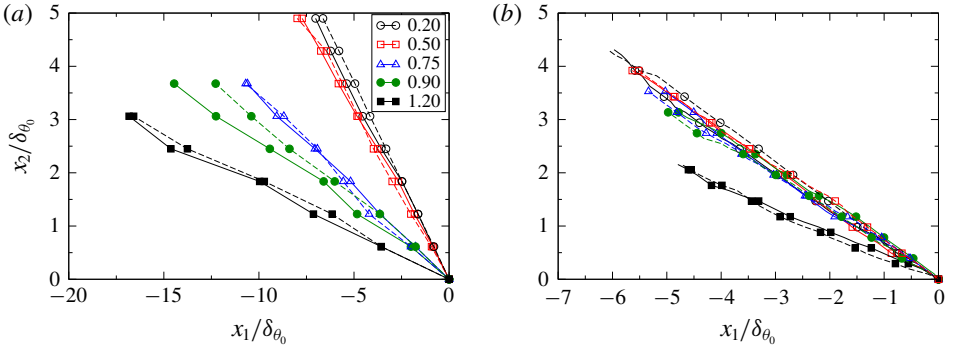

FIGURE 21. (Colour online) Projections of the most probable orientation of vortex vectors for different M_c at (*a*) $\tau = 100$ and (*b*) $\tau = 300$. The solid lines are constructed from the peaks of JPDF in quadrant II and the dashed lines from the peaks in quadrant IV.

vectors are closer to the x_1 axis than those at other Mach numbers. This applies to not only the most probable occurrence but also most of the orientations with large probabilities as discussed below.

With increasing Mach number the high probability regions (indicated in red) move closer towards $\cos\theta = \pm 1$, as seen in figure 19. The change is subtle as M_c increases from 0.50 to 0.90 but more prominent at the highest Mach number. This implies that the vortex vectors get more aligned along the streamwise direction as compressibility effects increase. The number of helical streamlines in the flow field, which are oriented in directions close to the streamwise direction, increases with increase in M_c. The JPDFs at a later time ($\tau = 300$) are shown in figure 22. The high probability regions occur at a smaller $|\cos\theta|$ in comparison with figure 19. This means that the vortex vectors tend to move away from the streamwise direction as time progresses. As seen in figure 21(*b*), by $\tau = 300$, the most probable orientations of the vortex vectors are less sensitive to compressibility effects, except for the largest M_c. In comparison with their orientations at $\tau = 100$, the vortex vectors tend to move away from directions closer to the streamwise direction. Nevertheless, more vortex vectors at a higher M_c continue to be closer to the streamwise direction than those at a lower M_c. This dependence of vortex vector orientation on the convective Mach number becomes clear when the probability density function of $\cos\theta$ is analysed. In figure 23, the probability density function of the magnitude of the cosine of the angle between vortex vector and streamwise direction is plotted at two different times. The vectors which are closely aligned towards the streamwise direction have larger values of $|\cos\theta|$ and those inclined away from the streamwise direction have smaller magnitudes of $\cos\theta$. In figure 23(*a*), which is at $\tau = 200$, there are more vectors which are aligned in (or opposite to) the direction of the streamwise axis at all Mach numbers. The higher the Mach number, the larger the PDF value for direction cosines close to unity, which implies that the probability of vectors being oriented in directions closer to the streamwise direction increases with M_c. A reverse trend can be seen at lower magnitudes of the cosines which are more likely to occur at lower convective Mach numbers. The PDF at a later time ($\tau = 300$) in figure 23(*b*) shows that while the likelihood of finding vortex vectors not close to the streamwise directions increases, there still exist more vectors which are closely aligned to the streamwise direction. The dependence of PDF on the convective Mach number also

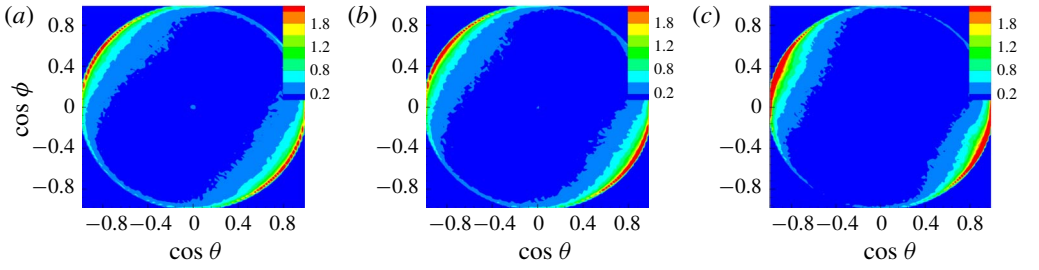

FIGURE 22. (Colour online) The JPDFs, $P(\theta, \phi)$, for different Mach numbers at $\tau = 300$ for vortex vectors in the region $-2\delta_\theta \leqslant x_2 \leqslant 2\delta_\theta$. (*a*) $M_c = 0.50$, (*b*) $M_c = 0.90$, (*c*) $M_c = 1.20$.

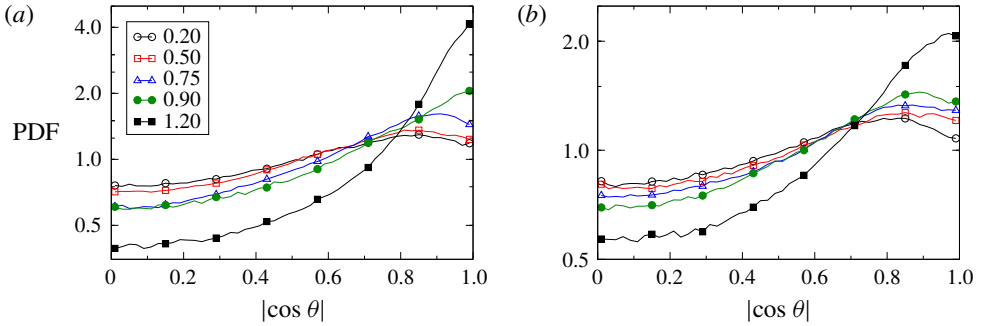

FIGURE 23. (Colour online) Probability density functions of absolute values of $\cos\theta$ at different M_c. (*a*) $\tau = 200$, (*b*) $\tau = 300$.

remains similar to that at earlier times. It can be inferred that the vortex vectors change their orientation as the flow evolves with more vectors getting inclined away from directions closer to the streamwise direction. For the incompressible Mach numbers, there are more vortex vectors at larger θ at earlier time instants. From figures 21 and 23, it is clear that, as time progresses, the vortical structures in the compressible cases approach the incompressible state. The solenoidal nature of velocity fluctuations in compressible shear flows during later times is observed by Bertsch *et al.* (2012). We can conclude that similar behaviour is exhibited by the flow structures too.

For completeness, we also report the statistics of the other two direction cosines. Figure 24 shows the JPDF, $P(\psi, \phi)$, for different Mach numbers at $\tau = 200$. It can be observed that it is rare to find vortex vectors with negative values of $\cos\psi$, which indicates that almost all of them have their spanwise components of vortex vector along the positive x_3 direction. In this work, the mixing-layer evolution is in such a way that the mean vorticity is along the positive spanwise direction. Thus the vortex vectors also tend to align in the direction of mean vorticity. The JPDF patterns are similar for the lower M_c, but for the highest M_c, the pattern is significantly different. At $M_c = 1.20$, the probability of finding vortex vectors being oriented with very small values of $\cos\psi$ and $\cos\phi$ is significant, as inferred from the green patch seen on the JPDF plot near the origin. In our earlier discussions, we have observed that at this Mach number, the probability of vortex vectors being aligned very close to the streamwise axis is very large. Therefore, those vectors are characterized by very small values of direction cosines for the other two directions, and this is reflected in the

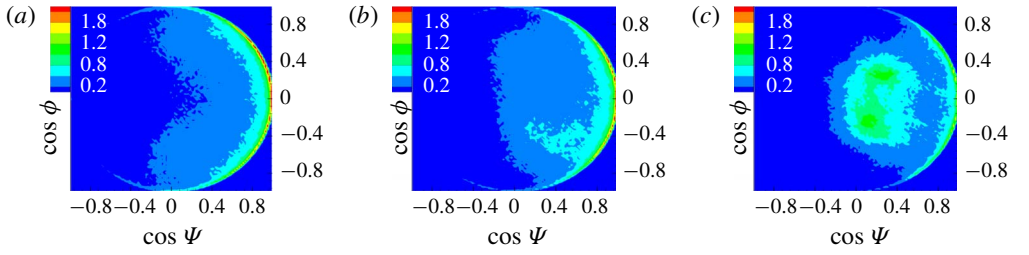

FIGURE 24. (Colour online) The JPDFs, $P(\psi, \phi)$, for different Mach numbers at $\tau = 300$ for vortex vectors in the region $-2\delta_\theta \leqslant x_2 \leqslant 2\delta_\theta$. (*a*) $M_c = 0.50$, (*b*) $M_c = 0.90$, (*c*)$M_c = 1.20$.

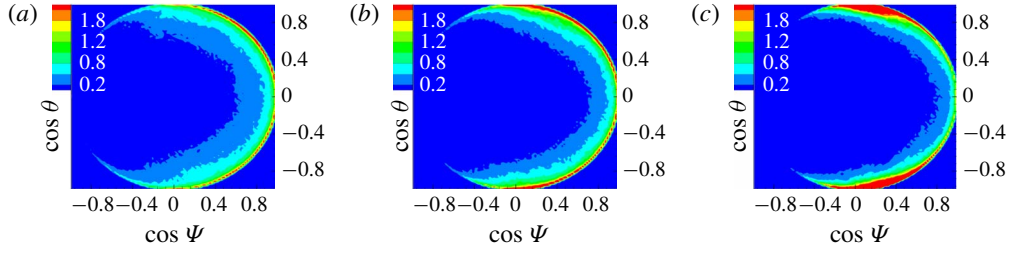

FIGURE 25. (Colour online) The JPDFs, $P(\psi, \theta)$, for different Mach numbers at $\tau = 300$ for vortex vectors in the region $-2\delta_\theta \leqslant x_2 \leqslant 2\delta_\theta$. (*a*) $M_c = 0.50$, (*b*) $M_c = 0.90$, (*c*) $M_c = 1.20$.

JPDF plot here. The JPDF of the remaining cosine pair, $P(\psi, \theta)$ is shown in figure 25. These JPDF plots also indicate that negative values of $\cos\psi$ are not so likely, and at higher Mach numbers the high probability orientations move towards $\cos\theta = \pm 1$. The orientations with respect to spanwise and transverse directions are also shown using the PDF of respective direction cosines in figure 26. The PDF of $|\cos\phi|$, shown in figure 26(*a*), implies that as Mach number increases, there are fewer vectors aligned in the transverse direction. The orientation of vectors with respect to the x_3 direction has a uniform distribution, to a moderate extent, at smaller M_c. At the highest M_c, as more and more vortices align in the streamwise direction, they are more likely to be orthogonal to the spanwise direction as indicated by the high PDF value for $|\cos\psi| \approx 0$ in figure 26(*b*). In the present results, the strength of rotation of vortical structures is given by the magnitude of vortex vector. Evolution of volume-averaged vortex strength for different cases is given in figure 27. The vortex strength (R) is normalized by the initial value (R_0). Vortex strength increases as the mixing layer develops. However, the strength of rotation of fluid elements is suppressed by compressibility. The vortical structures at high M_c mixing layers align in the streamwise direction but are weaker compared to those at low M_c.

In summary, vortex vectors tend to align more towards the streamwise direction as compressibility effects increase. This means that there are more helical streamline patterns in the flow field, which are aligned in such a way that the axes of helices are closer to the streamwise direction. The net turbulent transport of fluctuating momentum ($\overline{u_1'' u_2''}$) in those regions are less, as discussed above. Thus, more vortical structures getting aligned in the streamwise direction effectively brings down the turbulent stress R_{12} and decreases the turbulent kinetic energy production.

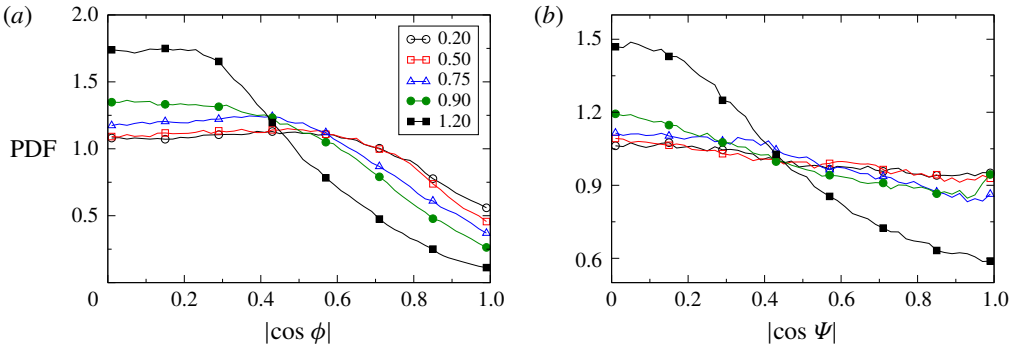

FIGURE 26. (Colour online) Probability density functions of absolute values of (*a*) $\cos\phi$ and (*b*) $\cos\psi$ at different M_c. The statistics are obtained at $\tau = 200$.

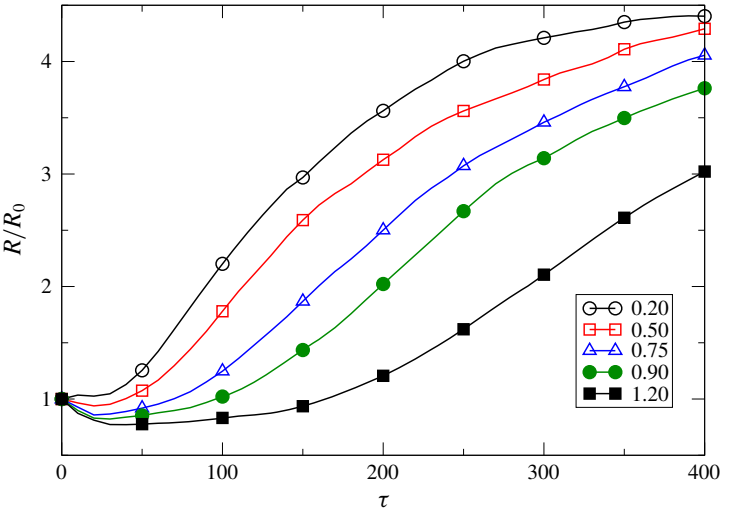

FIGURE 27. (Colour online) Evolution of volume-averaged vortex strength with time for different cases. Vortex strength, the magnitude of vortex vector, is normalized by the initial value.

Similar changes in vortical structures with compressibility have been observed by Normand & Lesieur (1992) during the transition in compressible boundary layers. The transitional flow at low Mach numbers is dominated by hairpin vortices and spanwise billows, but at high Mach numbers, they observed that there are Λ-vortices which break up into small-scale structures. Sandham & Reynolds (1990) reported the streamwise elongation of vortices in compressible mixing layers, as compressibility effects increase. These vortices are less intense compared to those at low M_c. The presence of more streamwise aligned vortical structures of lesser strength in our present study conforms to these results.

4. Conclusion

Direct numerical simulations of compressible mixing layers are performed for different Mach numbers, including a nearly incompressible case. The evolution of mixing-layer thickness and degree of suppression of growth rates by compressibility

are in agreement with existing numerical and experimental results. The primary objective of this work is to further enhance our understanding of the effects of compressibility on the transient evolution.

In the early evolution, the following are observed for turbulent statistics.

(i) Suppression of energy production and subsequently turbulent kinetic energy by compressibility during the transient development.
(ii) There exists a balance between R_{12} production and pressure rate of strain correlation (Π_{12}), which results in reduced levels of the Reynolds shear stress.
(iii) Compressibility also reduces the redistribution, which again causes suppression of energy production.

The present study reaffirms that the effects of compressibility vary with time and are more prominent during the transient evolution.

The topology is classified into two regions – strain dominated or vortex dominated – using the Q criterion. Influence of topology on the turbulent mechanism is examined using statistics conditioned on topology, which reveals the following.

(i) Redistribution of normal Reynolds stresses is higher in strain-dominated regions as compared to vortex-dominated topologies.
(ii) This leads to reduced levels of R_{12} and turbulent kinetic energy in vortex-dominated regions.
(iii) Compressibility alters local flow topology, resulting in a larger proportion of flow field having a vortex-dominated topology at higher M_c.

Since vortex-dominated regions are less energetic, a larger proportion of the same results in the suppression of turbulent kinetic energy as M_c increases. The volume fraction of vortex-dominated regions in the flow field approaches the incompressible value as time progresses (observed for all M_c).

Application of a recently developed vortex identification technique suggests a new interpretation of the correlations between turbulent energy production and streamline topology. We find that vortex-dominated regions feature helical streamline patterns which are associated with lower levels of turbulent production. Orientations of helical streamlines are quantified using the structure of vortex vector field, which gives the magnitude and direction of rotation of fluid elements in vortex-dominated regions. A statistical analysis of vortex vector orientation in the flow field shows that

(i) vortex vector orientations depend on compressibility;
(ii) at higher M_c, the vortical structures are more aligned in the streamwise direction whereas at lower M_c these structures align at considerably larger angles with the streamwise direction;
(iii) the orientations of vortical structures for all M_c shift to larger angles, similar to incompressible flow, with the progress in time;
(iv) the rate at which the orientation changes is decreasing with M_c.

Helical streamline patterns, with axes closer to the streamwise direction, are associated with small values of $\overline{u_1'' u_2''}$ and hence lower turbulent energy production. Therefore, the suppression of turbulent energy production is observed to be correlated with the presence of a large number of vortical structures aligned in the streamwise direction.

Acknowledgements

The authors acknowledge the High Performance Computing Environment Facility at IIT Madras for providing computing time on the VIRGO Super Cluster. This research

was supported in part by the International Centre for Theoretical Sciences (ICTS) during a visit for participating in the programme – Turbulence from Angstroms to light years (Code: ICTS/Prog-taly2018/01). The authors thank S. K. Lele for valuable discussions during the programme.

Appendix A. Numerical scheme and convergence

A.1. *BGK gas-kinetic scheme*

The numerical simulations are performed using a gas-kinetic scheme. The scheme uses a finite volume formulation to solve the Boltzmann equation with the Bhatnagar–Gross–Krook model for the collision integral (Xu *et al.* 2005). The BGK-Boltzmann equation is

$$\frac{\partial f}{\partial t} + c_i \frac{\partial f}{\partial x_i} = -\frac{f-g}{\tau}, \tag{A 1}$$

where f is velocity distribution function, g is equilibrium distribution function, c_i are the particle velocities and τ is average particle collision time. Equation (A 1) describes the evolution of the distribution function, which is a function of space x_i, time t, particle velocity c_i and internal variable ξ, in the absence of any external forces. The equilibrium distribution has the Maxwellian form and is a function of flow variables as follows:

$$g = \rho \left(\frac{\lambda}{\pi}\right)^{(K+2)/2} \exp[-\lambda((c_1-U_1)^2 + (c_2-U_2)^2 + (c_3-U_3)^2 + \xi^2)]. \tag{A 2}$$

In the above expression, ρ is the density, U_i are the macroscopic velocities and $\lambda = m/2kT$. The last term in the exponent has the form $\xi^2 = \xi_1^2 + \xi_2^2 + \cdots + \xi_K^2$, where K is the total number of internal degrees of freedom for the gas molecule given by $K = (5-3\gamma)/(\gamma-1)$. The flow variables, $W = (\rho, \rho\boldsymbol{U}, \rho\epsilon)^{\mathrm{T}}$, are related to f by

$$W = \begin{pmatrix} \rho \\ \rho U_1 \\ \rho U_2 \\ \rho U_3 \\ \rho\epsilon \end{pmatrix} = \int \psi_\alpha f \, \mathrm{d}\Xi, \tag{A 3}$$

where $\psi_\alpha = (1, c_1, c_2, c_3, \frac{1}{2}(c_1^2 + c_2^2 + c_3^2 + \xi^2))^{\mathrm{T}}$ are the weights and the integration is over the entire phase space $\mathrm{d}\Xi = \mathrm{d}c_1\mathrm{d}c_2\mathrm{d}c_3\mathrm{d}\xi_1\mathrm{d}\xi_2\cdots\mathrm{d}\xi_n$. Mass, momentum and energy conservation equations for compressible flows are recovered from the BGK-Boltzmann equation when $\tau = \mu/P$. The moments of (A 1) integrated over the phase space in a numerical cell and time step Δt give

$$\begin{aligned} W_{mnp}^{n+1} - W_{mnp}^{n} = \frac{1}{\Delta x_1 \Delta x_2 \Delta x_3} \int_{t^n}^{t^{n+1}} \Bigg[& \int (F_{m-1/2,n,p} - F_{m+1/2,n,p}) \, \mathrm{d}x_2 \, \mathrm{d}x_3 \\ & + \int (G_{m,n-1/2,p} - G_{m,n+1/2,p}) \, \mathrm{d}x_1 \, \mathrm{d}x_3 \\ & + \int (H_{m,n,p-1/2} - H_{m,n,p+1/2}) \, \mathrm{d}x_1 \, \mathrm{d}x_2 \Bigg] \, \mathrm{d}t. \end{aligned} \tag{A 4}$$

The time-dependent fluxes (F, G, H) of macroscopic quantities arise from the advection terms in the BGK-Boltzmann equation. The moments of the right-hand

side collision model vanish because mass, momentum and energy are conserved during particle collisions. This leads to the compatibility condition

$$\int \psi_\alpha (g - f)\, \mathrm{d}\Xi = 0. \tag{A 5}$$

For a cell (m, n, p), flux across a cell interface with normal in the x_1 direction is computed by

$$\begin{pmatrix} F_\rho \\ F_{\rho U_1} \\ F_{\rho U_2} \\ F_{\rho U_3} \\ F_{\rho \epsilon} \end{pmatrix} = \int c_1 \psi_\alpha f(x_1^{m+1/2}, x_2^n, x_3^p, t, c_i, \xi). \tag{A 6}$$

The distribution function used for computing the flux is given by the general solution of the BGK model at the cell interface, in terms of an initial distribution f_0 and the equilibrium state g. In our simulations, we use a second-order BGK scheme in which the distribution functions are linearly reconstructed around cell interfaces. For example, the distribution functions are reconstructed in the following way around the interface located at $x_1^{m+1/2}$,

$$f_0 = \begin{cases} g^l(1 + a^l x_1 + b^l x_2 + c^l x_3 - \tau(a^l c_1 + b^l c_2 + c^l c_3 + A^l)), & x_1 < x_1^{m+1/2}, \\ g^r(1 + a^r x_1 + b^r x_2 + c^r x_3 - \tau(a^r c_1 + b^r c_2 + c^r c_3 + A^r)), & x_1 > x_1^{m+1/2}. \end{cases} \tag{A 7}$$

The coefficients a^l, a^r are associated with gradients of flow variables normal to the interface and b^l, ..., c^r with gradients tangential to the interface. Equilibrium distributions g^l and g^r correspond to the reconstructed values of macroscopic variables on either side of the interface. Macroscopic variables are reconstructed using a weighted essentially non-oscillatory scheme following Kumar *et al.* (2013). This enables us to resolve any sharp discontinuities like shocklets in the turbulent flow field. All simulations are carried out with $Pr = 0.7$. The Prandtl number correction is applied at the step where coefficients $a^l, a^r, \ldots$ are calculated. This does not change the underlying BGK scheme and is equivalent to dividing the heat flux term by the Prandtl number in a conventional Navier–Stokes solver (May *et al.* 2007).

The equilibrium distribution is reconstructed as

$$g = g_0[1 + (1 - h[x - x_1^{m+1/2}])\bar{a}^l x_1 + h[x_1 - x_1^{m+1/2}]\bar{a}^r x_1 + bx_2 + cx_3 + \bar{A}t], \tag{A 8}$$

where g_0 is the local equilibrium distribution at the interface, $h(x)$ is the Heaviside function which is one for positive values of x and zero otherwise. The coefficients are calculated from the gradients of flow variables. Coefficients A^l and A^r are obtained by equating the moments of non-equilibrium contributions in (A 7) to zero and $\bar{A}$ from the compatibility condition (A 5). The procedure to obtain these coefficients from gradients of flow variables can be found in Xu *et al.* (2005). After determining these parameters, the distribution function at the cell interface, which is used to compute the numerical flux, is given by

$$\begin{aligned} f(x_1^{m+1/2}, x_2^n, x_3^p, t, c_i, \xi) \;=\; & (1 - e^{-t/\tau})g_0 + \tau(t/\tau - 1 + e^{-t/\tau})\bar{A}g_0 \\ & + (\tau(-1 + e^{-t/\tau}) + te^{-t/\tau}) \end{aligned}$$

Case	M_c	L_1/δ_{θ_0}	L_2/δ_{θ_0}	L_3/δ_{θ_0}	$N_1 \times N_2 \times N_3$
M12	1.20	314.16	157.08	78.54	$512 \times 256 \times 128$
LD12	1.20	314.16	157.08	157.08	$512 \times 256 \times 128$
HR12	1.20	314.16	157.08	78.54	$768 \times 384 \times 192$

TABLE 3. Grid details for the high resolution and larger spanwise extent simulations.

$$\begin{aligned}&\times (\bar{a}^l h[c_1]\bar{a}^r(1-h[c_1]) + \bar{b}c_2 + \bar{c}c_3)c_1 g_0\\ &+ e^{-t/\tau}\,([1-(t+\tau)(c_1a^l + c_2b^l + c_3c^l)]h[c_1]g^l\\ &+ [1-(t+\tau)(c_1a^r + c_2b^r + c_3c^r)](1-h[c_1])g^r)\\ &- e^{-t/\tau}(\tau A^l h[c_1]g^l + \tau A^r(1-h[c_1])g^r).\end{aligned} \tag{A 9}$$

Flux across the interface $m+1/2$ is computed by substituting (A 9) in (A 6). A similar procedure is used to calculate fluxes G and H in the other two directions.

The time advancement is included in the flux calculation according to equation (A 4) by way of an exact integration in time of the discretized distribution function. The resulting scheme is second order accurate in time, as shown in Ohwada (2002). The time step used in this integration is calculated using the CFL criterion by

$$\Delta t = C\frac{\mathcal{V}}{\Sigma_k(\lambda_c S_k + 2\lambda_v S_k^2/\mathcal{V})}, \tag{A 10}$$

where C is the CFL number, $\mathcal{V}$ is the volume of the cell, S_k is the area of the kth face of the cell, $\lambda_c = |U_k| + c_s$ and $\lambda_v = \gamma\nu/Pr$. The quantities U_k and c_s are the face-normal velocity and speed of sound. The stability of the scheme depends on the macroscopic flow variables as in the case of Navier–Stokes solvers (Venugopal & Girimaji 2015).

A.2. *Convergence of the numerical simulations*

Two additional simulations are performed to check the accuracy of the results. The additional simulations are for the largest convective Mach number to examine the effects of grid resolution and spanwise domain extent. The initial conditions for these simulations are the same as that for the case M12 reported in this work. The details of the high resolution (HR12) and larger domain (LD12) grids are given in table 3 Case LD12 has a spanwise extent twice as that in the other two cases. The domain is uniformly discretized with equal spacing in all three directions.

The results from LD12 and HR12 simulations are compared with those of M12. The momentum thickness evolution in these simulations does not show any significant difference, as can be seen in figure 28(*a*). The focus of this work is the transient evolution of the mixing layer. The evolution of averaged turbulent kinetic energy, calculated using equation (3.4), is shown in figure 28(*b*). As in the case of momentum thickness, the turbulent kinetic energy is not influenced by the domain extent or the cell size. The Reynolds stress anisotropy also shows grid and domain independence (see figure 28*c*).

The effects of domain extent and grid resolution on the topology dependence of the turbulent statistics are also investigated. Figure 29 shows that the shear-dominated regions have more turbulent kinetic energy than vortex-dominated regions irrespective of the domain extent and grid resolution. It is also important to show that the

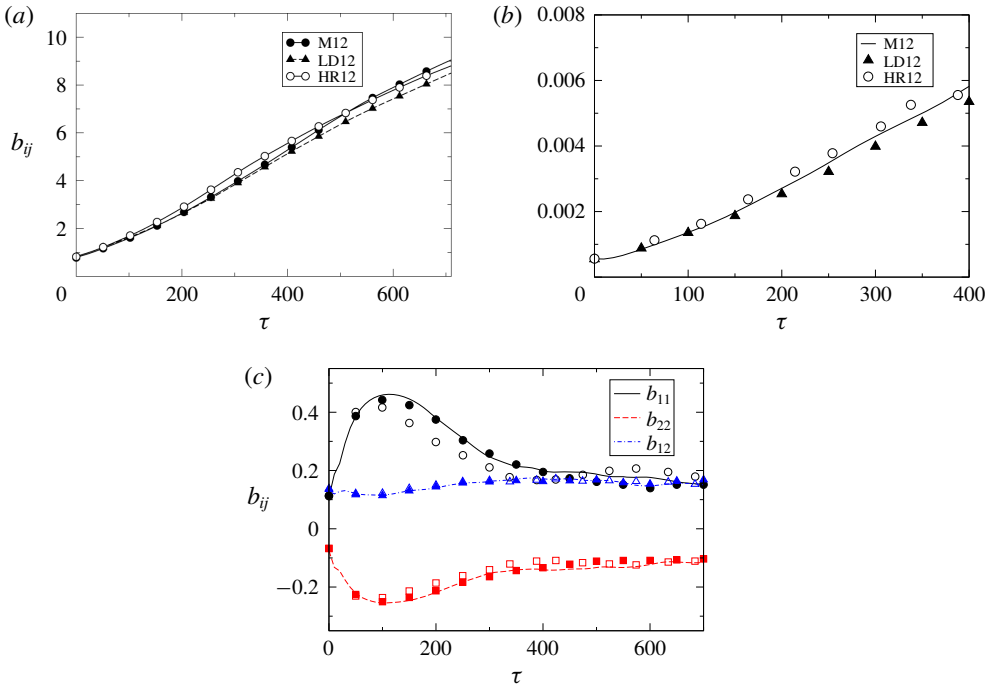

FIGURE 28. (Colour online) (*a*) Momentum thickness evolution with time for the three simulations. (*b*) Evolution of turbulent kinetic energy with time. (*c*) Evolution of anisotropy tensor. Solid line and circles, b_{11}; dashed line and squares, b_{22}; dot-dashed line and triangles, b_{12}. Filled and unfilled symbols correspond to LD12 and HR12 simulations, respectively.

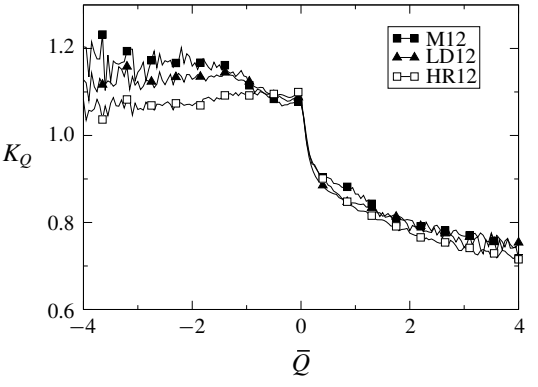

FIGURE 29. Conditionally averaged turbulent kinetic energy for different simulations at $\tau = 340$.

topology of the flow is grid converged. For this purpose, we compare the fraction of vortex-dominated topology in the flow field from different simulations. The cases M12, LD12 and HR12 respectively have 42, 43 and 41 per cent of the flow field with a vortex topology at the instant $\tau = 340$. The contours of vorticity on the streamwise plane during the evolution of M12 and LD12 are shown in figure 30. The spanwise

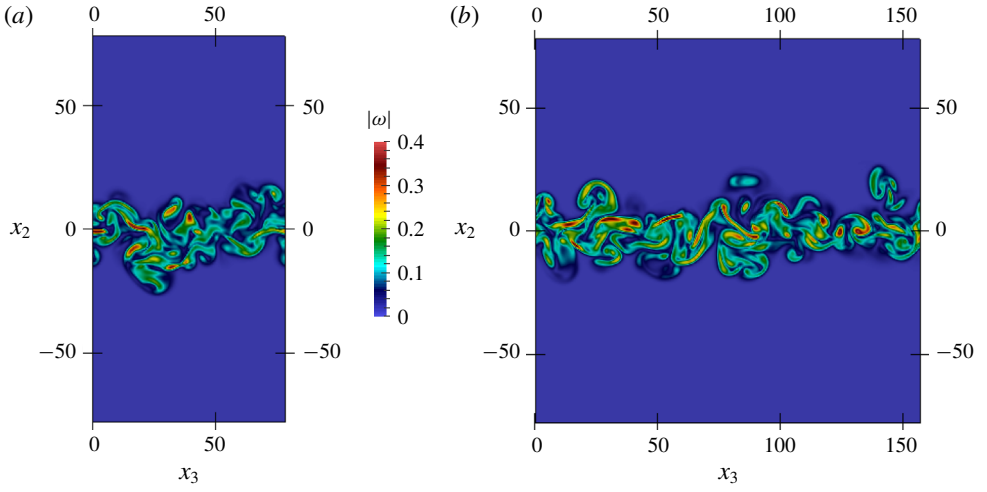

FIGURE 30. (Colour online) Vorticity contours on the x_2x_3 plane at $\tau = 400$. (*a*) M12 and (*b*) LD12.

distributions of vortical structures are not influenced by the length of the domain. From these results, it can be seen that HR12 and LD12 simulations do not differ significantly from M12. Hence, it is concluded that the resolutions and domains used for M12 and other simulations are adequate for the present work.

Appendix B. Helical streamlines and velocity correlation

Consider the parametric equation for a helix (streamline) given by

$$\boldsymbol{r}(t) = (At, B\sin t, B\cos t), \tag{B 1}$$

where A and B are constants. The tangent vector for this curve is

$$\boldsymbol{u}'' = (A, B\cos t, -B\sin t), \tag{B 2}$$

which is the local velocity. When the helical streamline has the axis along x_1, as in figure 16(*a*), the components of the tangent vector are equal to the velocity components in the original coordinate system (x_1, x_2, x_3), given by

$$u_1'' = A; \quad u_2'' = B\cos t. \tag{B 3a,b}$$

The velocity correlation is obtained by the average of the product $u_1''u_2''$. Over one period of the helix,

$$\overline{u_1''u_2''} = \frac{\displaystyle\int_0^{2\pi} u_1''u_2''\,\mathrm{d}t}{\displaystyle\int_0^{2\pi}\mathrm{d}t} = \frac{\displaystyle\int_0^{2\pi} AB\cos t\,\mathrm{d}t}{\displaystyle\int_0^{2\pi}\mathrm{d}t} = 0. \tag{B 4}$$

In figure 16(*b*), the axis of the helix is at an angle θ with respect to x_1. Velocity components in the original coordinate system (x_1, x_2, x_3) are given by

$$\begin{pmatrix} u_1'' \\ u_2'' \\ u_3'' \end{pmatrix} = \begin{bmatrix} \cos\theta & -\sin\theta & 0 \\ \sin\theta & \cos\theta & 0 \\ 0 & 0 & 1 \end{bmatrix} \begin{pmatrix} A \\ B\cos t \\ -B\sin t \end{pmatrix}. \tag{B 5}$$

Then,

$$u_1'' = A\cos\theta - B\cos t\sin\theta; \quad u_2'' = A\sin\theta + B\cos t\cos\theta, \tag{B 6a,b}$$

$$u_1''u_2'' = A^2\sin\theta\cos\theta + AB\cos^2\theta\cos t - B^2\cos^2 t\sin\theta\cos\theta, \tag{B 7}$$

for which

$$\int_0^{2\pi} u_1''u_2''\,\mathrm{d}t \neq 0, \tag{B 8}$$

over a period of the helix. The velocity correlation is thus non-zero and hence also the production. This indicates that the reduction in turbulent energy production is strongly correlated with the orientation of helical streamlines.

REFERENCES

BARONE, M. F., OBERKAMPF, W. L. & BLOTTNER, F. G. 2006 Validation case study: prediction of compressible turbulent mixing layer growth rate. *AIAA J.* **44** (7), 1488–1497.

BIRCH, S. F. & EGGERS, J. M. 1972 A critical review of experimental data for developed free turbulent shear flows. In *Free Turbulent Shear Flows*, vol. I, pp. 11–40. NASA SP-321.

BERTSCH, R. L., SUMAN, S. & GIRIMAJI, S. S. 2012 Rapid distortion analysis of high Mach number homogeneous shear flows: characterization of flow-thermodynamics interaction regimes. *Phys. Fluids* **24** (12), 125106.

CHONG, M. S., PERRY, A. E. & CANTWELL, B. J. 1990 A general classification of three-dimensional flow fields. *Phys. Fluids* A **2** (5), 765–777.

EPPS, B. 2017 Review of vortex identification methods. In *AIAA SciTech Forum*. American Institute of Aeronautics and Astronautics.

FOYSI, H. & SARKAR, S. 2010 The compressible mixing layer: An LES study. *Theor. Comput. Fluid Dyn.* **24** (6), 565–588.

FREUND, J. B., LELE, S. K. & MOIN, P. 2000 Compressibility effects in a turbulent annular mixing layer. Part 1. Turbulence and growth rate. *J. Fluid Mech.* **421**, 229–267.

FU, S. & LI, Q. 2006 Numerical simulation of compressible mixing layers. *Intl J. Heat Fluid Flow* **27** (5), 895–901.

GATSKI, T. & BONNET, J. P. 2013 *Compressibility, Turbulence and High Speed Flow*. Academic Press.

HADJADJ, A., YEE, H. C. & SJÖGREEN, B. 2012 LES of temporally evolving mixing layers by an eighth-order filter scheme. *Intl J. Numer. Meth. Fluids* **70** (11), 1405–1427.

HUNT, J. C. R., WRAY, A. A. & MOIN, P. 1988 Eddies, streams, and convergence zones in turbulent flows. In *Proceedings of the Center for Turbulence Research Summer Program CTR-S88*. Stanford University.

JAHANBAKHSHI, R. & MADNIA, C. K. 2016 Entrainment in a compressible turbulent shear layer. *J. Fluid Mech.* **797**, 564–603.

JAHANBAKHSHI, R., VAGHEFI, N. S. & MADNIA, C. K. 2015 Baroclinic vorticity generation near the turbulent/non-turbulent interface in a compressible shear layer. *Phys. Fluids* **27** (10), 105105.

JEONG, J. & HUSSAIN, F. 1995 On the identification of a vortex. *J. Fluid Mech.* **285**, 69–94.

KARIMI, M. & GIRIMAJI, S. S. 2016 Suppression mechanism of Kelvin-Helmholtz instability in compressible fluid flows. *Phys. Rev.* E **93**, 041102.

KARIMI, M. & GIRIMAJI, S. S. 2017 Influence of orientation on the evolution of small perturbations in compressible shear layers with inflection points. *Phys. Rev.* E **95**, 033112.

KOLÁR, V. 2009 Compressibility effect in vortex identification. *AIAA J.* **47** (2), 473–475.

KUMAR, G., GIRIMAJI, S. S. & KERIMO, J. 2013 WENO-enhanced gas-kinetic scheme for direct simulations of compressible transition and turbulence. *J. Comput. Phys.* **234**, 499–523.

LAVIN, T. A., GIRIMAJI, S. S., SUMAN, S. & YU, H. 2012 Flow-thermodynamics interactions in rapidly-sheared compressible turbulence. *J. Theor. Comput. Fluid Dyn.* **26** (6), 501–522.

LEE, K. & GIRIMAJI, S. S. 2013 Flow-thermodynamic interactions in decaying anisotropic compressible turbulence with imposed temperature fluctuations. *J. Theor. Comput. Fluid Dyn.* **27**, 115–131.

LELE, S. K. 1994 Compressibility effects on turbulence. *Annu. Rev. Fluid Mech.* **26**, 211–254.

LIU, C., GAO, Y., TIAN, S. & DONG, X. 2018 Rortex – A new vortex vector definition and vorticity tensor and vector decompositions. *Phys. Fluids* **30** (3), 035103.

MA, Z. & XIAO, Z. 2016 Turbulent kinetic energy production and flow structures in compressible homogeneous shear flow. *Phys. Fluids* **28** (9), 096102.

MAY, G., SRINIVASAN, B. & JAMESON, A. 2007 An improved gas-kinetic BGK finite-volume method for three-dimensional transonic flow. *J. Comput. Phys.* **220** (2), 856–878.

MOIN, P. & KIM, J. 1985 The structure of the vorticity field in turbulent channel flow. Part. I – Analysis of istantaneous fields and statistical correlations. *J. Fluid Mech.* **155**, 441–464.

NORMAND, X. & LESIEUR, M. 1992 Direct and large-eddy simulations of transition in the compressible boundary layer. *J. Theor. Comput. Fluid Dyn.* **3** (4), 231–252.

OHWADA, T. 2002 On the construction of kinetic schemes. *J. Comput. Phys.* **177** (1), 156–175.

ONG, L. & WALLACE, J. M. 1998 Joint probability density analysis of the structure and dynamics of the vorticity field of a turbulent boundary layer. *J. Fluid Mech.* **367**, 291–328.

PANTANO, C. & SARKAR, S. 2002 A study of compressibility effects in the high-speed turbulent shear layer using direct simulation. *J. Fluid Mech.* **451**, 329–371.

PAPAMOSCHOU, D. & ROSHKO, A. 1988 The compressibile turbulent shear layer: an experimental study. *J. Fluid Mech.* **197**, 453–477.

PIROZZOLI, S., BERNARDINI, M., MARIÉ, S. & GRASSO, F. 2015 Early evolution of the compressible mixing layer issued from two turbulent streams. *J. Fluid Mech.* **777**, 196–218.

POPE, S. B. 2000 *Turbulent Flows*. Cambridge University Press.

ROGERS, M. M. & MOIN, P. 1987 The structure of the vorticity field in turbulent channel flow. *J. Fluid Mech.* **176**, 33–66.

SANDHAM, N. D. & REYNOLDS, W. C. 1990 Compressible mixing layer-linear theory and direct simulation. *AIAA J.* **28** (4), 618–624.

SANDHAM, N. D. & REYNOLDS, W. C. 1991 Three-dimensional simulations of large eddies in the compressible mixing layer. *J. Fluid Mech.* **224**, 133–158.

SARKAR, S., ERLEBACHER, G., HUSSAINI, M. Y. & KREISS, H. O. 1991 The analysis and modelling of dilatational terms in compressible turbulence. *J. Fluid Mech.* **227**, 473–493.

SLESSOR, M. D., ZHUANG, M. & DIMOTAKIS, P. E. 2000 Turbulent shear-layer mixing; growth-rate compressibility scaling. *J. Fluid Mech.* **414**, 35–45.

SORIA, J., SONDERGAARD, R., CANTWELL, B. J., CHONG, M. S. & PERRY, A. E. 1994 A study of the fine-scale motions of incompressible time-developing mixing layers. *Phys. Fluids* **6**, 871–884.

SUMAN, S. & GIRIMAJI, S. S. 2010 Velocity gradient invariants and local flow-field topology in compressible turbulence. *J. Turbul.* **11** (2), 1–24.

TIAN, S., GAO, Y., DONG, X. & LIU, C. 2018 Definitions of vortex vector and vortex. *J. Fluid Mech.* **849**, 312–339.

VAGHEFI, N. S. & MADNIA, C. K. 2015 Local flow topology and velocity gradient invariants in compressible turbulent mixing layer. *J. Fluid Mech.* **774**, 67–94.

VAGHEFI, N. S., NIK, M. B., PISCIUNERI, P. H. & MADNIA, C. K. 2013 A priori assessment of the subgrid scale viscous/scalar dissipation closures in compressible turbulence. *J. Turbul.* **14** (9), 43–61.

VENUGOPAL, V. & GIRIMAJI, S. S. 2015 Unified gas kinetic scheme and direct simulation Monte Carlo computation of high-speed lid driven microcavity flows. *Commun. Comput. Phys.* **17** (5), 1127–1150.

WANG, L. & LU, X. Y. 2012 Flow topology in compressible turbulent boundary layer. *J. Fluid Mech.* **703**, 255–278.

WHITE, F. M. 2006 *Viscous Fluid Flow*. McGraw-Hill.

XU, K., MAO, M. & TANG, L. 2005 A multidimensional gas-kinetic BGK scheme for hypersonic viscous flow. *J. Comput. Phys.* **203** (2), 405–421.

ZHOU, Q., HE, F. & SHEN, M. Y. 2012 Direct numerical simulation of a spatially developing compressible plane mixing layer: flow structures and mean flow properties. *J. Fluid Mech.* **711**, 437–468.